USGS
science for a changing world

Global Mineral Resource Assessment

Regional Mapping of Hydrothermally Altered Igneous Rocks Along the Urumieh-Dokhtar, Chagai, and Alborz Belts of Western Asia Using Advanced Spaceborne Thermal Emission and Reflection Radiometer (ASTER) Data and Interactive Data Language (IDL) Logical Operators—A Tool for Porphyry Copper Exploration and Assessment

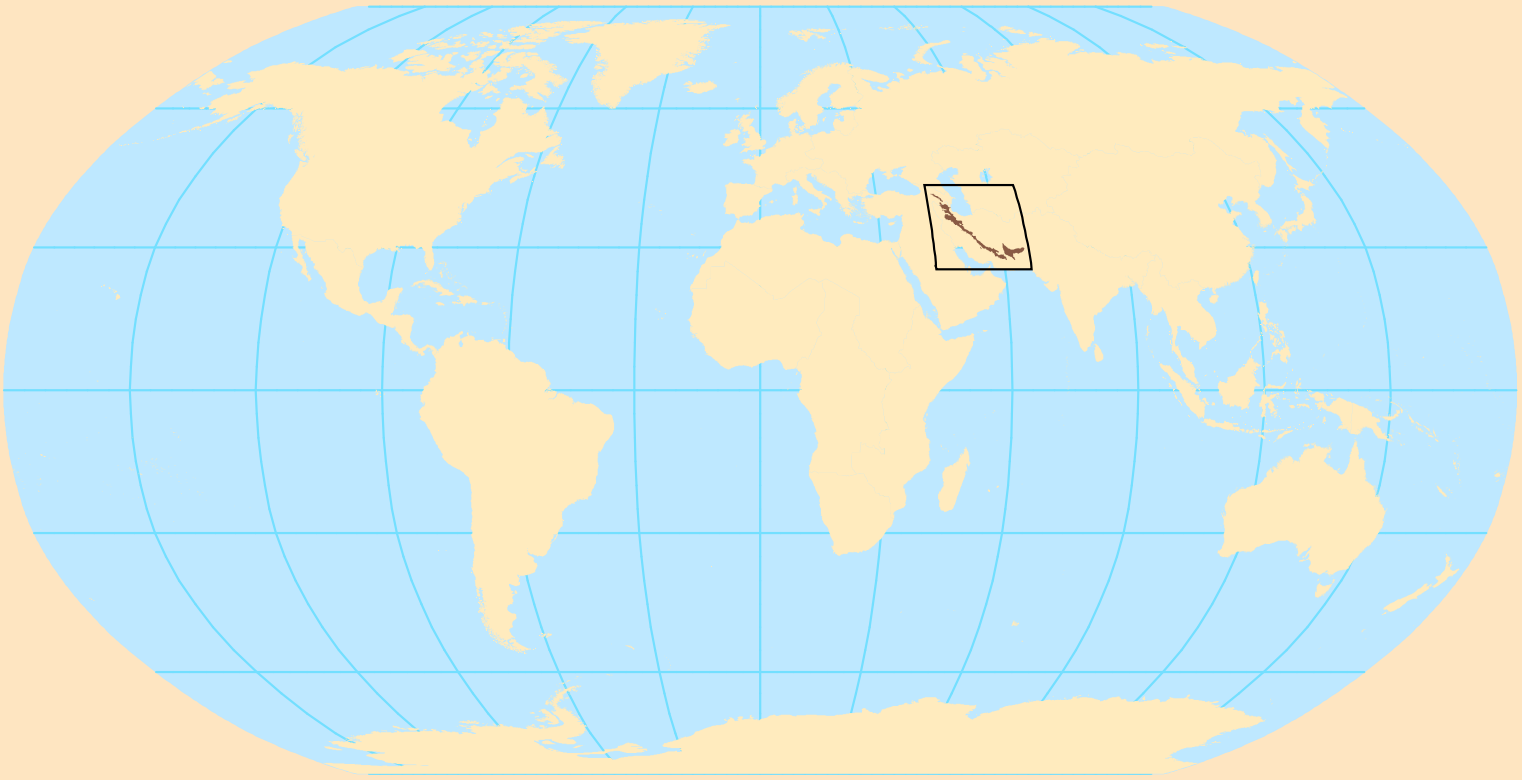

Scientific Investigations Report 2010–5090–O

U.S. Department of the Interior
U.S. Geological Survey

This page left intentionally blank.

Global Mineral Resource Assessment

Michael L. Zientek, Jane M. Hammarstrom, and Kathleen M. Johnson, editors

Regional Mapping of Hydrothermally Altered Igneous Rocks Along the Urumieh-Dokhtar, Chagai, and Alborz Belts of Western Asia Using Advanced Spaceborne Thermal Emission and Reflection Radiometer (ASTER) Data and Interactive Data Language (IDL) Logical Operators—A Tool for Porphyry Copper Exploration and Assessment

By John C. Mars

Scientific Investigations Report 2010–5090–O

U.S. Department of the Interior
U.S. Geological Survey

U.S. Department of the Interior
SALLY JEWELL, Secretary

U.S. Geological Survey
Suzette M. Kimball, Acting Director

U.S. Geological Survey, Reston, Virginia: 2014

Suggested citation:
Mars, J.C., 2014, Regional mapping of hydrothermally altered igneous rocks along the Urumieh-Dokhtar, Chagai, and Alborz Belts of western Asia using Advanced Spaceborne Thermal Emission and Reflection Radiometer (ASTER) data and Interactive Data Language (IDL) logical operators—A tool for porphyry copper exploration and assessment: U.S. Geological Survey Scientific Investigations Report 2010–5090–O, 36 p., 10 plates, and spatial data, available at *http://dx.doi.org/10.3133/sir201050900*.

ISSN 2328-0328 (online)

Contents

Figures

Tables

Plates

[Available online only at http://pubs.usgs.gov/sir/2010/5090/o/]

9. Map of Potential Porphyry Copper Sites and ASTER Hydrothermal Alteration in the South-Central Urumieh-Dokhtar Volcanic Belt, South-Central Iran
10. Map of Potential Porphyry Copper Sites and ASTER Hydrothermal Alteration in the Southeastern Urumieh-Dokhtar and Chagai Volcanic Belts, Southeastern Iran, Southwestern Pakistan, and Southern Afghanistan

Conversion Factors

Inch/Pound to SI

Multiply	By	To obtain
	Length	
inch (in.)	2.54	centimeter (cm)
inch (in.)	25.4	millimeter (mm)
inch (in.)	25,400	micrometer (μm)
foot (ft)	0.3048	meter (m)
mile (mi)	1.609	kilometer (km)
mile, nautical (nmi)	1.852	kilometer (km)
yard (yd)	0.9144	meter (m)
	Area	
acre	4,047.0	square meter (m^2)
acre	0.4047	hectare (ha)
acre	0.4047	square hectometer (hm^2)
acre	0.004047	square kilometer (km^2)
square foot (ft^2)	929.0	square centimeter (cm^2)
square foot (ft^2)	0.09290	square meter (m^2)
square inch (in^2)	6.452	square centimeter (cm^2)
section (640 acres or 1 square mile)	259.0	square hectometer (hm^2)
square mile (mi^2)	259.0	hectare (ha)
square mile (mi^2)	2.590	square kilometer (km^2)

SI to Inch/Pound

	Length	
centimeter (cm)	0.3937	inch (in.)
millimeter (mm)	0.03937	inch (in.)
micrometer (μm)	0.00003937	inch (in.)
meter (m)	3.281	foot (ft)
kilometer (km)	0.6214	mile (mi)
kilometer (km)	0.5400	mile, nautical (nmi)
meter (m)	1.094	yard (yd)
	Area	
hectare (ha)	2.471	acre
hectare (ha)	0.003861	square mil (mi^2)
square meter (m^2)	0.0002471	acre
square hectometer (hm^2)	2.471	acre
square kilometer (km^2)	247.1	acre
square centimeter (cm^2)	0.001076	square foot (ft^2)
square meter (m^2)	10.76	square foot (ft^2)
square centimeter (cm^2)	0.1550	square inch (ft^2)
square kilometer (km^2)	0.3861	square mile (mi^2)

Vertical coordinate information is referenced to the World Geodetic System WGS84.

Horizontal coordinate information is referenced to the World Geodetic System WGS84.

Altitude, as used in this report, refers to distance above the vertical datum.

Acronyms and Abbreviations Used

AMB	Alborz magmatic belt
ASTER	Advanced Spaceborne Thermal Emission and Reflection Radiometer
AVIRIS	Airborne Visible Infrared Imaging Spectrometer
CVB	Chagai volcanic belt
GIS	geographic information system
IDL	Interactive Data Language
LO	logical operator
MODIS	Moderate Resolution Imaging Spectroradiometer
SSIB	small-scale digital international boundaries
SWIR	short-wave near infrared
TIR	thermal infrared
UDVB	Urumieh-Dokhtar volcanic belt
USGS	U.S. Geological Survey
VNIR	visible near infrared

Regional Mapping of Hydrothermally Altered Igneous Rocks Along the Urumieh-Dokhtar, Chagai, and Alborz Belts of Western Asia Using Advanced Spaceborne Thermal Emission and Reflection Radiometer (ASTER) Data and Interactive Data Language (IDL) Logical Operators—A Tool for Porphyry Copper Exploration and Assessment

By John C. Mars

Abstract

Regional maps of phyllic and argillic hydrothermal alteration were compiled using Advanced Spaceborne Thermal Emission and Reflection Radiometer (ASTER) data and logical operator algorithms. The area mapped extends from northwestern Iran to southeastern Pakistan and includes volcanic and magmatic arcs that make up the Urumieh-Dokhtar volcanic belt (UDVB), the Chagai volcanic belt (CVB), and the central part of the Alborz magmatic belt (AMB). The volcanic belts span the Zagros-Makran transform zone and the present day Baluchistan (Makran) volcanic arc. ASTER visible near infrared (VNIR) data contain three bands between 0.52 and 0.86 micrometers (μm) and the short-wave infrared (SWIR) data consist of six bands spanning 1.6 to 2.43 μm with 15-meter (m), and 30-m resolution, respectively.

During the 8-year project, three different calibration methods were used to correct ASTER SWIR anomalies and produce ASTER calibrated reflectance data, which were then used to map hydrothermally altered rocks. Logical operators, used to map hydrothermally altered rocks, perform multiple band ratios and thresholds that can be applied to multiple ASTER scenes using a single algorithm, thus eliminating separate production and application of vegetation and dark pixel masks. Argillic and phyllic band ratio logical operators use band ratios that define the 2.17- and 2.20-μm absorption features to map kaolinite and alunite, typical in argillized rocks, and muscovite, which is a common mineral in phyllic alteration. Band thresholds for ratios in argillic and phyllic logical operator algorithms were determined by mapping known argillic and phyllic rocks at a calibration test site in Cuprite, Nevada, in the United States.

The regional argillic and phyllic hydrothermal alteration map and geologic and deposit maps of the study area illustrate that distinct patterns of altered rocks are typically associated with certain types of mineral deposits. The central part of the UDVB contains numerous circular to elliptical patterns (1 to 5 kilometers in diameter) of mapped phyllic- and argillic-altered rocks associated with Eocene to Miocene intrusive igneous rocks, some of which host known porphyry copper deposits such as at Meiduk, Sar Cheshmeh, and Seridune in Iran. The Zagros-Makran transform zone and areas adjacent to the Saindak porphyry deposit and Taftan Volcano contain primarily phyllic-altered rocks that form linear patterns associated with extensive faulting and fractures indicative of epithermal and (or) polymetallic vein deposits.

The ASTER alteration map and corresponding geologic maps were used to select circular to elliptical patterns of argillic- and phyllic-altered volcanic and intrusive rocks as potential porphyry copper sites. One hundred and seventy eight potential porphyry copper sites were mapped along the UDVB, and 23 sites were mapped along the CVB. The potential sites were selected to assist in further exploration and assessments of undiscovered porphyry copper deposits.

Introduction

Porphyry copper deposits are typically characterized by zoned assemblages of hydrothermal alteration minerals (Lowell and Guilbert, 1970; fig. 1). Many of these minerals exhibit spectral absorption features in the visible near infrared (VNIR) through the short-wave near infrared (SWIR) (0.4 to 2.5 micrometers, µm; fig. 2) and the thermal-infrared (8.0 to 14.0 µm) wavelength regions (Abrams and others, 1983; Mars, 2010; Spatz and Wilson, 1995). The Advanced Spaceborne Thermal Emission and Reflectance Radiometer (ASTER) has sufficient spectral and spatial resolution to delineate spectral absorption features that can be used to identify and remotely map these alteration zones in well-exposed terrain (Mars, 2010). ASTER measures reflected radiation in three bands in the 0.52- to 0.86-µm wavelength region (VNIR); six bands in the 1.6- to 2.43-µm wavelength region (SWIR); and five bands of emitted radiation in the 8.125- to 11.65-µm wavelength region (TIR) with 15-, 30-, and 90-m resolution, respectively (Fujisada, 1995). ASTER also has a backward-looking VNIR telescope with 15-m resolution. Thus, stereoscopic VNIR images can be acquired at 15-m resolution. The swath-width is 60 kilometers (km), but off-nadir pointing capability extends the total cross-track viewing of ASTER to 232 km (Fujisada, 1995).

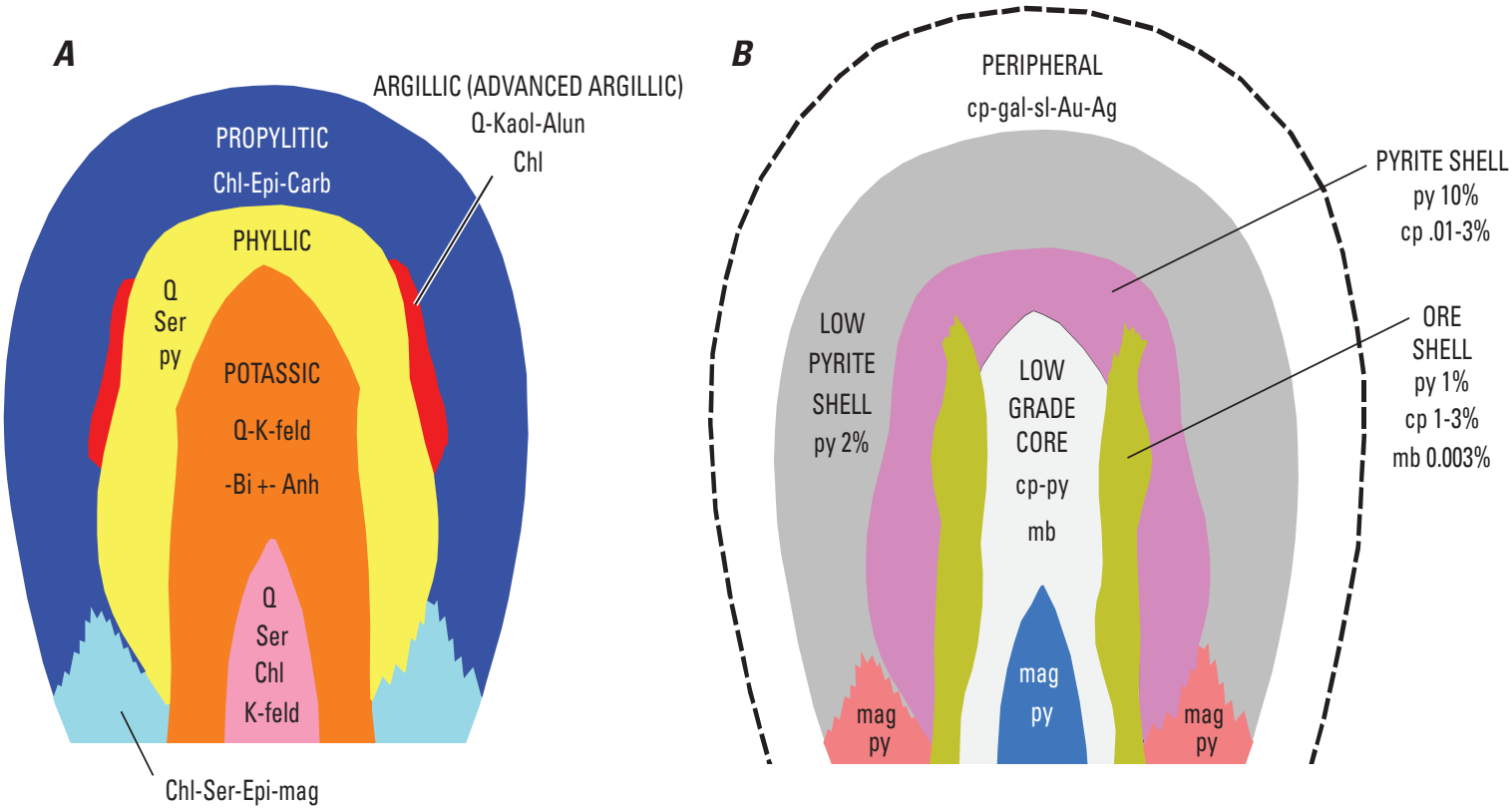

EXPLANATION

Chl - Chlorite	**Bi - Biotite**	**gal - Galena**
Epi - Epidote	**Anh - Anhydrite**	**sl - Sulfide**
Carb - Carbonate	**py - Pyrite**	**Au - Gold**
Q - Quartz	**Kaol - Kaolinite**	**Ag - Silver**
Ser - Sericite	**Alun - Alunite**	**mb - Molybdenite**
K-feld - Potassium feldspar	**cp - Chalcopyrite**	**mag - Magnetite**

Figure 1. Illustrated deposit model of a porphyry copper deposit (modified from Lowell and Guilbert, 1970). *A*, Schematic cross section of hydrothermal alteration minerals and types, which include propylitic, phyllic, argillic, and potassic alteration. *B*, Schematic cross section of ores associated with each alteration type. %, percent.

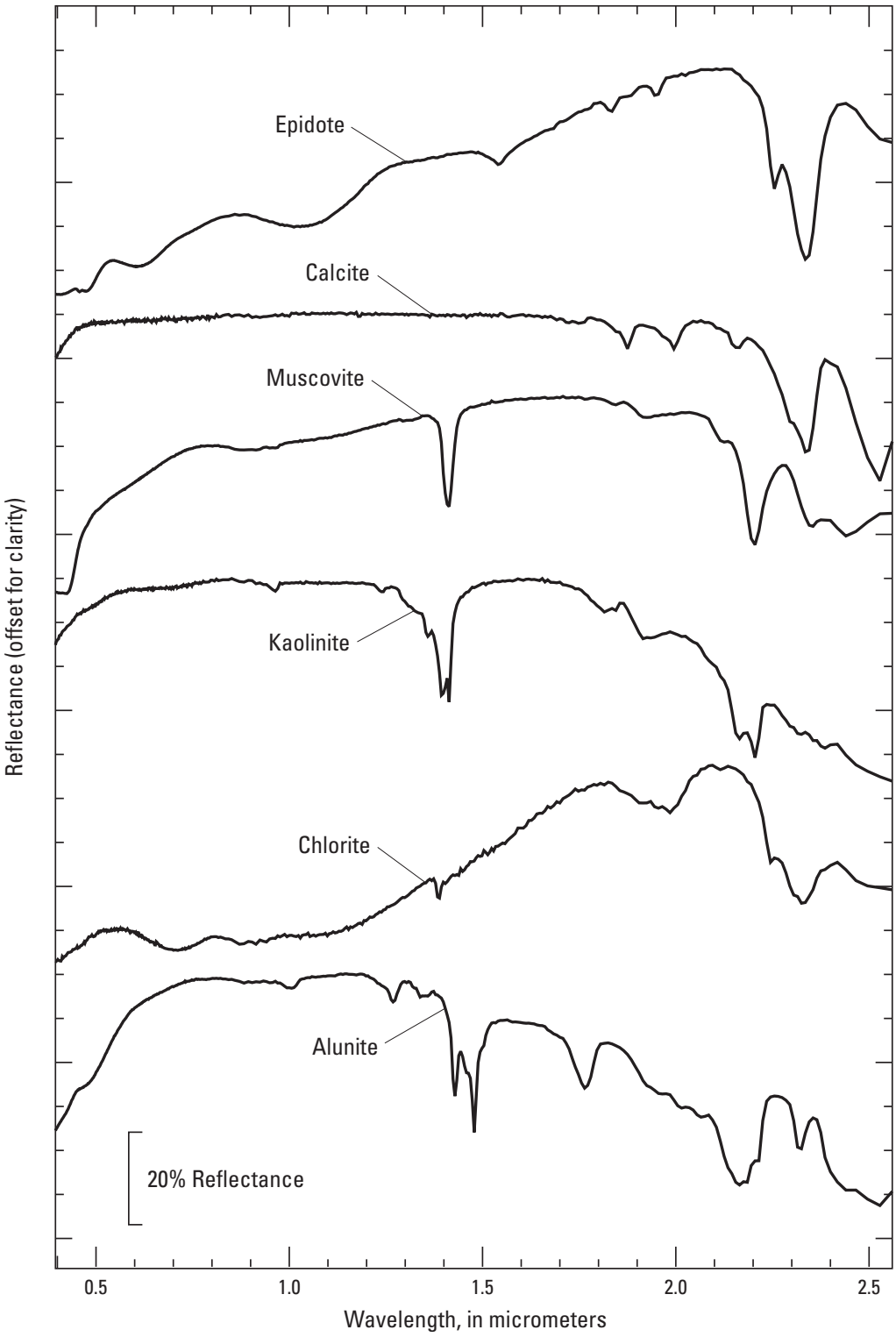

Figure 2. Laboratory spectra of epidote, calcite, muscovite, kaolinite, chlorite, and alunite, which are common hydrothermal alteration minerals (Clark and others, 1993b; Mars and Rowan, 2006). Alunite and kaolinite have Al-O-H absorption features at 2.17 and 2.20 micrometers (μm). Muscovite has a prominent Al-O-H 2.20-μm absorption feature and a secondary 2.35-micrometer absorption feature. Chlorite and epidote have a Fe-Mg-O-H 2.32-μm absorption feature and a broad Fe^{2+} feature from 1.65 to 0.6 micrometers. Calcite has a prominent 2.33-μm CO_3 absorption feature. %, percent.

The purpose of this study was to compile regional argillic and phyllic hydrothermal alteration maps for the Urumieh-Dokhtar volcanic belt (UDVB), the Chagai volcanic belt (CVB), and the Alborz magmatic belt (AMB) of western Asia. In addition, the alteration maps were used to select potential porphyry copper sites in the UDVB and CVB for use in a global assessment of porphyry copper (fig. 3). This paper describes (1) the relation between VNIR and SWIR spectral reflectance and alteration mineral assemblages associated with porphyry copper deposits, (2) calibration and mapping methods of ASTER data for regional mapping of hydrothermally altered rocks, (3) accurate geometric registration of the ASTER results, (4) the criteria for selecting potential porphyry copper sites, and (5) site locations and characteristics for each volcanic belt.

The UDVB, CVB, and AMB extend from northwest Iran through southeastern Pakistan and southern Afghanistan (fig. 3; Perelló and others, 2008; Shamanian and others, 2004). This region was selected for evaluation because of the extensive exposures of major porphyry copper deposits that include deposits at Sar Cheshmeh, Meiduk, Reko Diq, and Saindak (fig. 4; Singer and others, 2008). The study area receives approximately 140 millimeters (mm) of annual precipitation and, thus, has excellent bedrock exposure with minimal vegetation (http://www.climate-charts.com/World-Climate-Maps.html#rain, accessed October 17, 2013). In addition, field-compiled hydrothermal alteration maps at Sar Cheshmeh and Seridune and previous hydrothermal alteration mapping of the Sar Cheshmeh, Seridune, Reko Diq, and Meiduk mines using ASTER and Landsat Thematic Mapper (TM) data also provide validation for the regional mapping algorithms tested in this study (Barzegar, 2007; Mars, 2010; Ranjbar and others, 2004; Rowan and others, 2006; Tangestani and Moore, 2002; Waterman and Hamilton, 1975).

ASTER scene file numbers are listed in an Excel file as appendix A. A table of physical characteristics of potential porphyry copper sites is included as an Excel file in appendix B. Appendix C describes the spatial data files (Environmental Systems Research Institute, Inc., (Esri) geodatabase feature classes, an Esri map document, and shapefiles) that accompany this report.

Geology

The magmatic and volcanic arcs that make up the UDVB, CVB and AMB are the products of Tethys oceanic plate being subducted underneath the Iranian microplate followed by continent-to-continent collision of the Arabian and Eurasian Plates, subduction of Indian oceanic crust, and the collision of India with the southern margin of Eurasia, respectively (Perelló and others, 2008; Regard and others, 2004; Shamanian and others, 2004; Walker and Jackson, 2001). In southeastern Iran, the Zagros-Makran transform zone separates the older Cenozoic arc rocks from active subduction and volcanism of the Neogene Baluchistan volcanic arc (fig. 3; Regard and others, 2004). The Baluchistan Arc partially covers the southwestern part of the UDVB and extends across the CVB.

Most of the rocks that make up the northeastern and central parts of the UDVB consist of a volcanic succession of Eocene calc-alkaline basaltic andesite and Oligocene shoshonitic rock intruded by Neogene quartz diorite, quartz monzonite, and granodiorite that contain mined deposits of copper (Huber, 1969a,b; Hassanzadeh, 1993). Additional plutonic rocks include granite and gabbro, and volcanic rocks include basalt, andesite, and dacite, which were erupted as lava flows, ignimbrites, and pyroclastic flows (Huber, 1969a,b; Hassanzadeh, 1993). Most of the volcanism occurred from the Eocene to the Miocene (Huber, 1969a,b; Dimitrijevic, 1973; Hajian, 1977; Amidi, 1984). Extensive mineralization occurred from the Miocene to the Pliocene and produced porphyry- and vein-style mineralization. Large porphyry copper mines in the region include Sar Cheshmeh, in a quartz monzonite pluton, and Meiduk, in a quartz diorite pluton (Hassanzadeh, 1993). East of the Zagros-Makran transform zone the southeastern part of the UDVB consists primarily of Quaternary andesite and basalt, which are the products of the Baluchistan volcanic arc (fig. 3; Huber, 1969b). Less-extensive Paleogene volcanic rocks are dispersed around the periphery of the Quaternary intermediate volcanic rocks. Some of the Paleogene volcanic rocks are highly faulted and contain copper deposits (Huber, 1969b; Taghizadeh and Mallakpour, 1976).

Igneous rocks of the CVB consist primarily of Eocene to Pleistocene basalt and andesite intruded by Eocene granodiorite and quartz monzonite batholiths in the Chagai Hills and Miocene-Pliocene calc-alkaline, biotite- and amphibole-bearing porphyry quartz diorite and granodiorite stocks in the central and western parts of the volcanic belt (fig. 3; Perelló and others, 2008). There are a total of 48 mapped porphyry systems in the CVB that include large deposits at Sain Dak and Reko Diq (Perelló and others, 2008).

The volcanic rocks of the southern AMB consist primarily of Eocene andesite and dacite intruded by granodiorite and diorite (Alavi and Hushmandazdeh, 1976; Huber, 1977; Shamanian and others, 2004). In the central part of the magmatic belt, copper deposits are found in dacites, and epithermal gold veins are found in altered andesitic flows (Alavi and Hushmandazdeh, 1976; Shamanian and others, 2004).

Remote-Sensing Characteristics of Porphyry Copper Deposits and ASTER Data

Porphyry copper deposits in the southwestern United States typically consist of a core of quartz and potassium-bearing minerals, mostly potassium feldspar (K-feldspar) and biotite, surrounded by multiple zones of alteration minerals (fig. 1). The hydrous zones are characterized by mineral

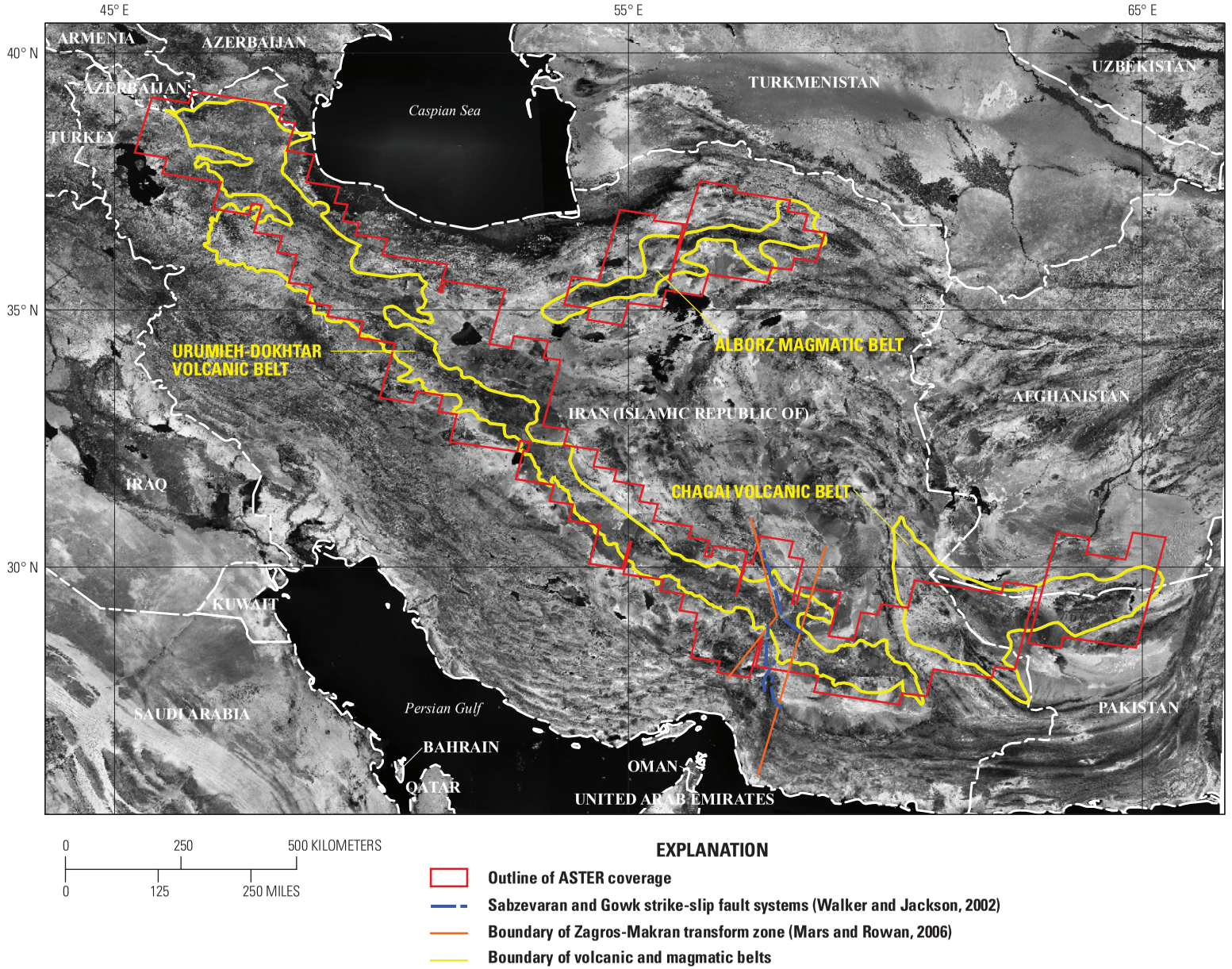

Figure 3. Location map of the Tertiary Urumieh-Dokhtar and Chagai volcanic belts and Alborz magmatic belt (yellow outline) and outline of Advanced Spaceborne Thermal Emission and Reflection Radiometer (ASTER) scenes (red outline) used to map hydrothermally altered rocks in western Asia. The Sabzevaran and Gowk strike-slip fault systems (blue dashed lines) and the Makran transfer zone are defined as the Zagros-Makran transform zone (orange lines), which defines the western limit of recent volcanism of the Neogene Baluchistan volcanic arc (Mars and Rowan, 2006; Regard and others, 2004; Walker and Jackson, 2001). Background image is a Landsat TM mosaic of band 7 (NASA, 2003).

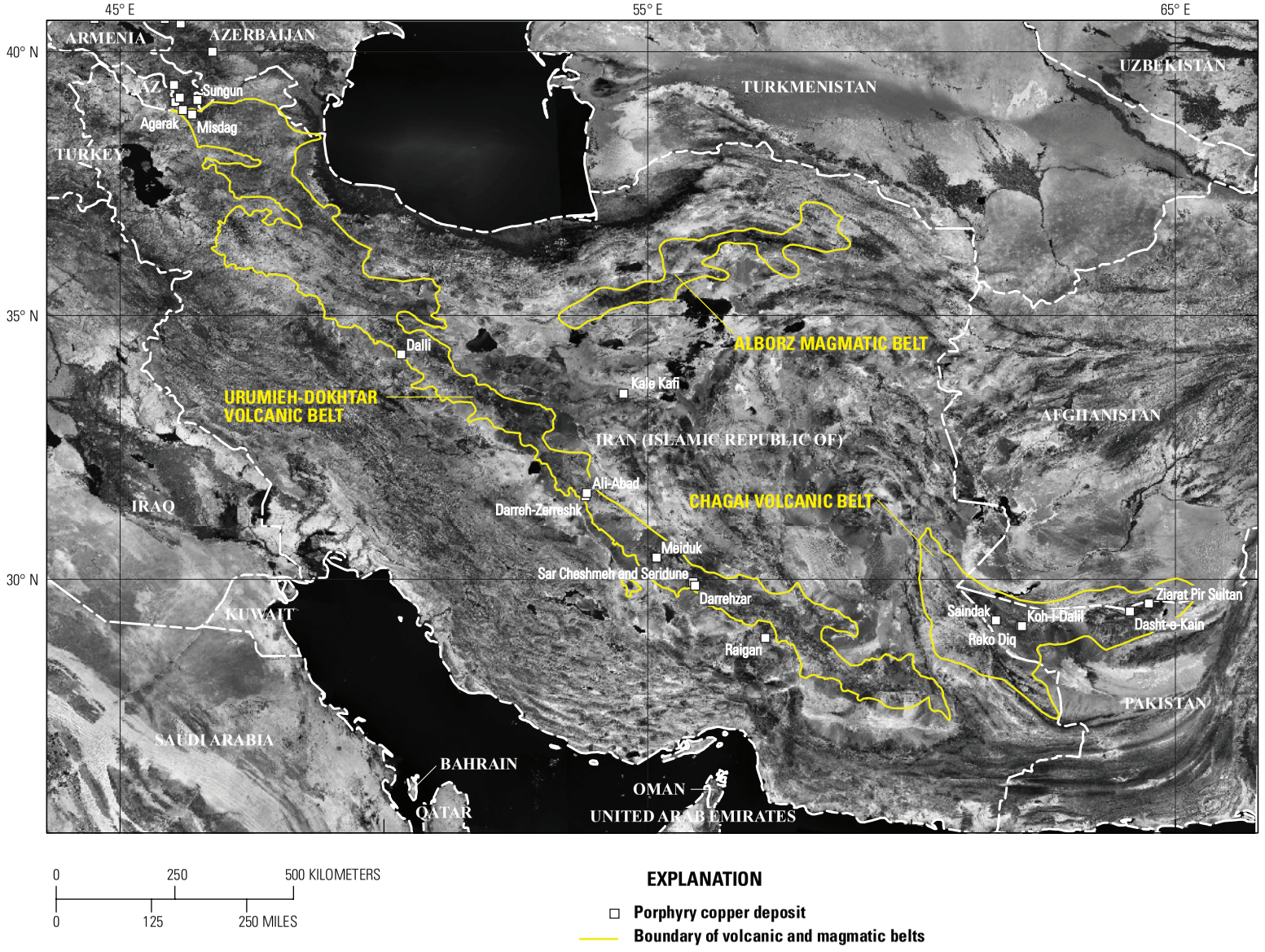

Figure 4. Location map of porphyry copper deposits in the study area in western Asia (Barzegar, 2007; Singer and others, 2008). Background image is a Landsat TM mosaic of band 7 (NASA, 2003).

assemblages that contain at least one mineral that exhibits diagnostic spectral absorption features. The broad phyllic zone, which is commonly limonitic due to oxidation of pyrite, is characterized by illite/muscovite (sericite), and the narrower argillic zone which typically consists of kaolinite and alunite (fig. 1; Abrams and Brown, 1984; Spatz and Wilson, 1995). The mineral assemblage of the outer propylitic zone is more variable to country rock compositional differences, but epidote, chlorite, and carbonate minerals are common constituents (fig. 1). Country rock and intrusive rock can host copper mineralization, and both can be hydrothermally altered (Titley, 1972). Additional factors that affect the surface exposure and spectral reflectance characteristics of these mineral assemblages are vegetation cover, topography, structural configuration, and anthropogenic activities. This analysis of ASTER data concentrates on the phyllic and argillic alteration zones because of the greater variability of the propylitic mineral assemblage and the lack of diagnostic VNIR-SWIR spectral absorption features within the core alteration zone.

Phyllic alteration spectral characteristics include illite/muscovite reflectance spectra that exhibit an intense Al-OH absorption feature, which is typically centered at 2.20 μm (ASTER band 6), and a less intense feature near 2.38 μm (ASTER band 8) (figs. 2 and 5). Argillic rocks, including rocks classified as advanced argillic, also display an Al-OH absorption feature near 2.20 μm, but both kaolinite and alunite exhibit significantly different spectral shape compared to muscovite/illite (figs. 2 and 5) (Hunt, 1977; Hunt and Ashley, 1979; Rowan and others, 2003). Kaolinite displays a secondary feature or shoulder at 2.17 μm and a minimum at 2.20 μm, whereas alunite exhibits a minimum at 2.17 μm (ASTER band 5) and a minor feature at 2.20 μm (figs. 2 and 5). These spectral differences are detectable in ASTER data at SWIR bands 4, 5, 6, and 7, respectively (fig. 5).

The spectral reflectance characteristics of phyllic, argillic, and propylitic rocks provide a basis for distinguishing hydrothermally altered rocks associated with porphyry copper deposits from most country rock lithologies, but ambiguities may result where the country rock contains the same minerals that are typical of altered rocks. For example, limonitic quartz-muscovite schist could be confused with phyllically altered rocks, and kaolinitic weathering surfaces might resemble argillized rocks spectrally. Thus, consideration of the compositional range of the country rock and their spectral reflectance is an important aspect of the analysis.

Study Methods

Production and Calibration of ASTER Reflectance Data

Comparisons of spectra from field samples to ASTER image reflectance spectra show spectral variations in the SWIR region caused by applying incorrectly calculated SWIR radiance coefficients and stray light leakage from band detector 4 into band detectors 5 and 9, which is defined as “Crosstalk” (Mars and Rowan, 2006, 2010). To correct these anomalies, three calibration methods were developed over a period of 8 years to produce accurately calibrated ASTER reflectance data for mapping argillic and phyllic hydrothermal alteration. The first calibration method was used on data covering southern Iran, the second method was used on data covering the Chagai Hills, and the third method calibrated ASTER data covering northern and southeastern Iran and southwestern Pakistan (plate 1, red—calibration method 1, magenta—calibration method 2, yellow—calibration method 3; note that plates are available online only at http://pubs.usgs.gov/sir/2010/5090/o/). All three methods produce similar results; however, the third method has the advantage of not needing spectral data from other spaceborne or airborne instruments, which may not be available for all areas of interest (Mars and Rowan, 2006, 2007, 2010). In each calibration method, the 30-m resolution SWIR data were resampled to 15 m to correspond to VNIR band spatial dimensions, and then the six SWIR and three VNIR bands were combined to form nine-band data sets with 15-m spatial resolution. All ASTER data were downloaded from the Land Process Distributed Active Archive Center (LP DAAC) located at the EROS Data Center, Sioux Falls, South Dakota.

Calibration Method 1

For the southern part of Iran, 56 AST_07 ASTER reflectance scenes were corrected using calibration method 1 (plate 1, red; appendix A). Each AST_07 scene consists of the nine ASTER VNIR-SWIR channels calibrated to reflectance using atmospherically corrected radiance at the surface data (Thome and others, 1999).

Comparisons of AST_07 ASTER reflectance data to spectra taken in situ from field samples and from calibrated hyperspectral data indicate anomalously low reflectance for ASTER band 5 (fig. 6; Mars and Rowan, 2006, 2010). If the reflectance in band 5 is too low, the spectra appear more similar in shape to argillic minerals such as alunite, and the mapping algorithms used in this study will map too much argillic alteration and not enough phyllic alteration (figs. 5 and 6).

Hyperion data were used to correct the ASTER AST_07 SWIR anomalies. Hyperion, a hyperspectral instrument flown on board the EO1 satellite platform, has 196 spectral bands in the 0.45 to 2.4 μm region (Kruse and others, 2003). Hyperion data can be properly calibrated to reflectance using the additional Hyperion atmospheric bands not available in ASTER data. Hyperion radiance data were calibrated to reflectance data using Atmospheric CORection Now (ACORN) atmospheric removal software (ImSpec, 2004) . In order to compare Hyperion reflectance data to ASTER reflectance data and to improve Hyperion’s signal to noise ratio, Hyperion reflectance data were resampled to ASTER VNIR-SWIR bandpasses. The ASTER-resampled Hyperion data were then georegistered to the orthorectified Landsat TM imagery (National Aeronautics and Space Administration, NASA, 2003; Tucker and others,

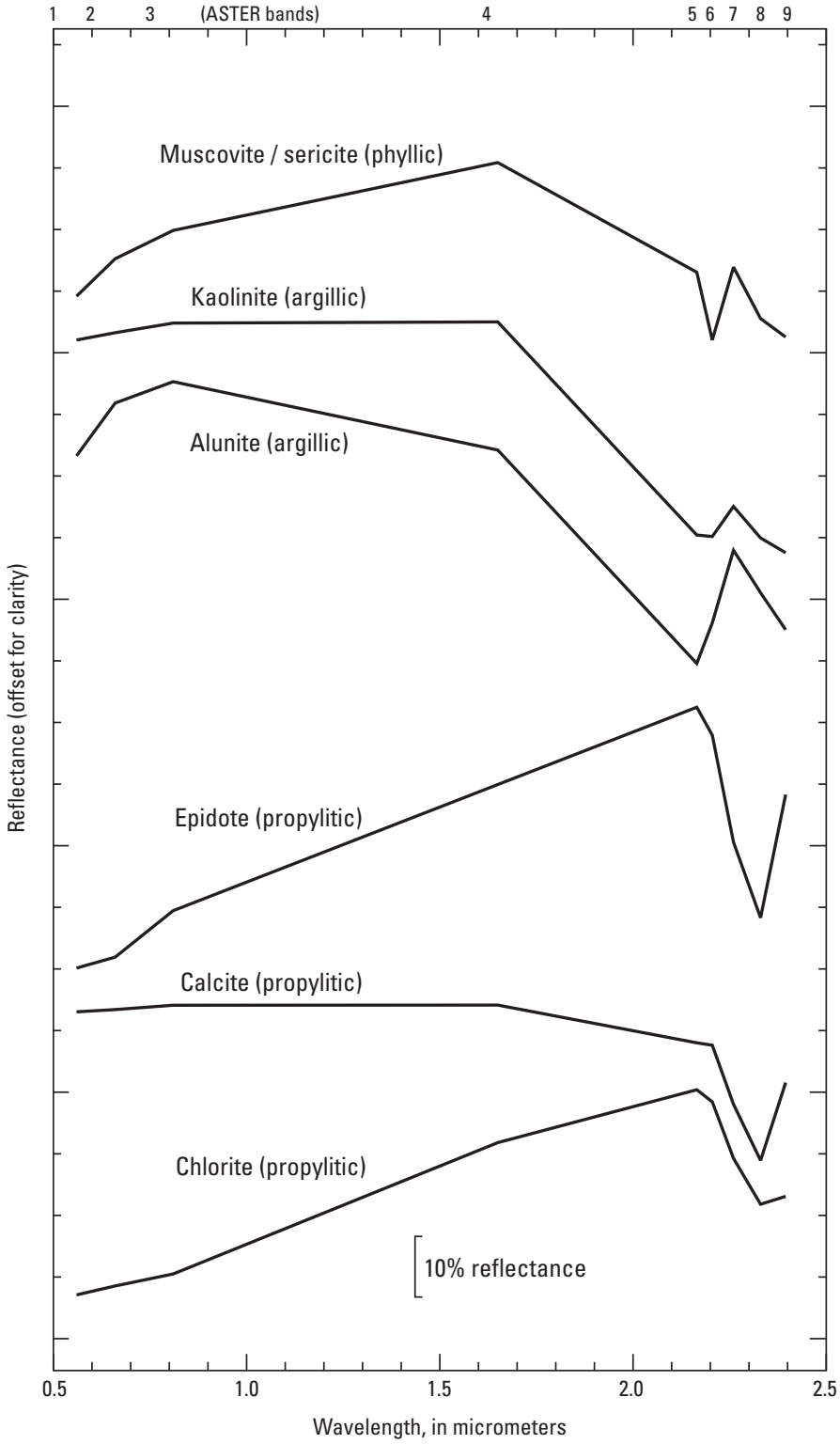

Figure 5. Laboratory spectra of muscovite/sericite (phyllic alteration mineral), kaolinite (argillic alteration mineral), alunite (argillic alteration mineral), epidote (propylitic alteration mineral), calcite (propylitic alteration mineral), and chlorite (propylitic alteration mineral) resampled to Advanced Spaceborne Thermal Emission and Reflection Radiometer (ASTER) bandpasses. The spectra illustrate the positions and intensities of absorption features in the 2.0–2.5-micrometer (μm) region used to define ratios in the argillic and phyllic mapping algorithms. The muscovite spectrum displays a 2.20-μm absorption feature at ASTER band 6, whereas kaolinite and alunite exhibit 2.17- and 2.20-μm micrometer absorption features at ASTER bands 5 and 6, respectively. Epidote, calcite and chlorite exhibit a 2.31–2.33-μm absorption feature at ASTER band 8. The numbers across the top of the graph indicate the ASTER band-center positions. Lab spectra from Clark and others (1993b). A scale of 10-percent (%) reflectance is shown on the plot.

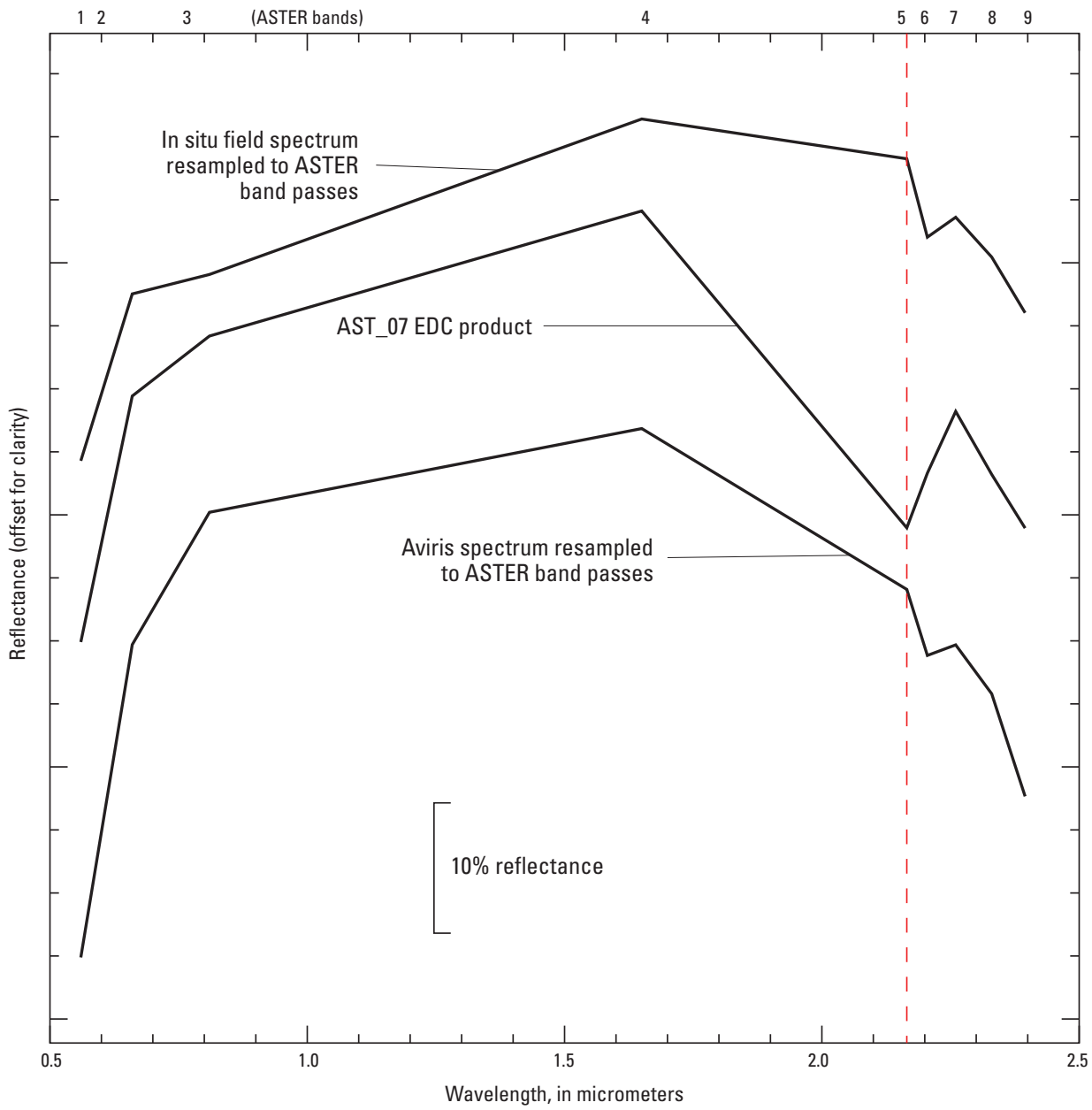

Figure 6. Spectra of playa from Cuprite, Nevada. Airborne Visible Infrared Imaging Spectrometer (AVIRIS) and in situ field spectra illustrate a slight 2.20 micrometer absorption feature. The AST_07 spectrum of the same playa illustrates that band 5 (red dashed line) is 10 to 15 percent lower than the AVIRIS or in situ field spectra in relation to band 6. The AST_07 spectrum erroneously has a similar shape to alunite spectra illustrated in figure 10. The numbers across the top of the graph indicate the Advanced Spaceborne Thermal Emission and Reflection Radiometer (ASTER) band center positions (from Mars and Rowan, 2006).

2004). Average spectra were extracted from areas of overlap between the ASTER and Hyperion scenes. A scalar correction consisting of the ASTER resampled Hyperion band ratio 5/6 divided by the ASTER band ratio 5/6 was applied to all ASTER band 5 data. A total of eight Hyperion scenes were used to correct the ASTER scenes calibrated using method 1. Difference ratios for the eight Hyperion scenes ranged from 5.8 to 10.3 percent with a standard deviation of 0.014325. Thus, an average of the scalar correction value (7.9 percent) was used to correct ASTER band 5 data for the scenes calibrated using method 1 (plate 1; appendix A).

Calibration Method 2

Fourteen ASTER Level_1b radiance scenes of southeastern Afghanistan and southwestern Pakistan that cover the Chagai Hills were converted to reflectance data using calibration method 2 (plate 1, magenta; appendix A). ASTER Level_1b radiance data contain all 15 ASTER bands spanning the VNIR, SWIR and TIR micrometer regions. The ASTER Level_1b VNIR and SWIR data were converted to reflectance data using atmospheric correction software and concurrent water vapor data obtained from the Moderate Resolution Imaging Spectrometer (MODIS; ImSpec, 2004). The MODIS instrument is on board the Terra satellite with the ASTER instrument and obtains data concurrently. MOD5_L2 data consist of 1 km pixel resolution column water vapor values (Gao and Kaufman, 1998). The MODIS MOD_05_L2 water vapor product was downloaded from the Goddard Space Flight Center using the Level 1 and Atmosphere Archive and Distribution System (LAADS; http://ladsweb.nascom.nasa.gov/data/search.html). The MODIS water vapor data were used to derive an average water vapor value for each ASTER scene from a small overlapping part of each MOD_05_L2 scene.

Hyperion reflectance data were used to correct for SWIR ASTER anomalies, as was done in calibration method 1. A total of 3 Hyperion scenes were used to correct the 14 ASTER scenes. An average of the scalar correction value (5.4 percent) was used to correct band 5 ASTER data for the study area.

Calibration Method 3

For areas covering northern and southern Iran and southwestern Pakistan, 101 ASTER Level_1b scenes were converted to reflectance data using calibration method 3 (plate 1, yellow; appendix A). In order to correct ASTER SWIR anomalies, the ASTER Level_1b data were crosstalk-corrected using the Iwasaki and Tonooka (2005) algorithm, converted from byte to radiance by applying radiometric conversion factors recorded in the Level_1B metadata, and radiometrically adjusted by applying Biggar and others' (2005) radiometric correction factors (fig. 6; Mars and Rowan, 2010). The ASTER reflectance data were compiled using the crosstalk-corrected and radiometrically corrected Level_1b data, a concurrent MODIS water vapor value, and an atmospheric correction program as were used in calibration method 2 and as described in a previous study by Mars and Rowan (2010; ImSpec, 2004).

Georegistration Correction

Individual ASTER scenes used in this study were recorded at four different viewing angles ranging from nadir to 8.2 degrees off nadir, which causes misregistration of as much as 600 m in high-relief terrain. Therefore, each ASTER nine-band reflectance dataset was geometrically registered to an orthorectified Landsat TM mosaic (NASA, 2003; Tucker and others, 2004). The Landsat TM mosaic data has a spatial resolution of 28 m and horizontal registration accuracy of ±50 m. Although this registration procedure corrected for the off-nadir viewing offset, the ASTER images were not corrected for terrain displacement. Using a first rotation or second order polynomial warp registration algorithm and at least nine ground control points for each scene produced root mean square (RMS) errors of less than 2.0 pixels (60 m). The Landsat 4 and 5 TM mosaic was also used as a base map to illustrate regional ASTER alteration for the study area (plates 2–10). Argillic and phyllic alteration units were converted to vector data, exported from the ASTER mineral maps as vector polygons and overlaid onto band 7 of the orthorectified Landsat TM mosaic (plates 2–10).

Logical Operator Mapping Algorithms

Logical operators (LO) are used in this study in order to streamline regional mapping and to consistently threshold band ratios used to map hydrothermally altered rocks for the entire study area. LO algorithms apply multiple band ratios and band thresholds to a scene using a single mathematical routine, thus, eliminating the separate production and application of band ratios, vegetation masks, and dark (noisy) pixel masks (table 1). Each LO determines a true or false value for each ratio by comparing the band ratio or threshold to a predetermined range of threshold values (table 1). For the selected ASTER bands and each ASTER pixel in a scene, all of the band ratios and thresholds in the algorithm have to be true in order for a value of 1 to be assigned to the pixel in an image; otherwise, a 0 value is assigned to the pixel. Thus, a byte image consisting of zeros and ones is produced by each algorithm. However, each of the three calibration methods produced reflectance datasets that required slightly different band ratio values in LO algorithms to map argillic and phyllic alteration (table 1). Band ratio values for each LO were determined for each calibration method using the Cuprite, Nevada, calibration-validation site, discussed in the following section. LO algorithms were developed using an Interactive Data Language (IDL) band math program in an imaging processing program (ITT, 2008).

All LO algorithms used in this study mask out green vegetation by utilizing the chlorophyll absorption feature at

0.65 µm by applying an ASTER 3/2 band ratio (fig. 7; table 1). Noisy, low reflectance pixels resulting from shadows, water, and mafic-ultramafic rocks were masked out using a maximum threshold of ASTER band 4. The argillic LO algorithms map the 2.165 and 2.2 µm Al-O-H absorption features using 4/6, 5/6, and 7/6 ratios (fig. 5; table 1). The phyllic LO algorithms also map the 2.2 µm Al-O-H absorption feature using 4/6, 5/6, and 7/6 ratios (fig. 5; table 1).

ASTER alteration units mapped using AST_07 ASTER data and calibration method 1 were median filtered using a three-by-three matrix to reduce noise (Mars and Rowan, 2006). Later calibration methods 2 and 3, which used ASTER Level_1b data converted to reflectance, produced less noisy mineral maps and did not need to be median filtered (Mars and Rowan, 2007, 2010).

Validation of Alteration Mapping Algorithms at the Cuprite, Nevada, Calibration/Validation Test Site

Cuprite, Nevada, was used as a site to test the accuracy the argillic and phyllic LO algorithms. Hydrothermal alteration has been mapped at Cuprite, Nevada, where argillic, opalized, and silicified alteration zones are laterally extensive (fig. 8; Ashley and Abrams, 1980; Swayze, 1997). Well-exposed, muscovite-rich Cambrian phyllitic siltstone bounds the western part of the hydrothermal alteration units (unit Ch; fig. 9). Although the phyllitic siltstones at Cuprite are not a product of hydrothermal alteration, they contain the same muscovite-rich mineralogy found in hydrothermally altered phyllic rocks. Previous mineral maps and spectral data from calibration and validation studies of hyperspectral and multispectral imaging detectors at Cuprite were used to evaluate the LO algorithm mapping results (Rowan and others, 2003; Clark and others, 1993a; Kruse and others, 2003).

The argillic and phyllic LOs for each calibration method produced similar results at Cuprite, Nevada (figs. 10 and 11). Two validation methods were used to test the accuracy of the argillic and phyllic LO algorithms at Cuprite. Both validation methods used mineral maps compiled from Airborne Visible Infrared Imaging Spectrometer (AVIRIS) data for comparison to ASTER derived mineral maps. AVIRIS is an airborne hyperspectral sensor with 224 spectral bands in the 0.45- to 2.4-µm region and 20-m spatial resolution (Green and others, 1998). Previous studies at Cuprite illustrate that AVIRIS can accurately map minerals with Al-OH absorption features (Clark and others, 1993a; Clark and Swayze 1996).

Table 1. Logical operator algorithms used to map argillic- and phyllic-altered rocks in Iran, Pakistan, and Afghanistan.

Alteration type	Algorithm
	Method 1—southern Iran
Argillic	((float(b3)/b2) le 1.35) and (b4 gt 260) and ((float(b4)/b6) gt 1.25) and ((float(b5)/b6) le 1.05) and ((float(b7)/b6) ge 1.03)
Phyllic	((float(b3)/b2) le 1.35) and (b4 gt 260) and ((float(b4)/b6) gt 1.25) and ((float(b5)/b6) gt 1.05) and ((float(b7)/b6) ge 1.03)
	Method 2—southern Afghanistan and southern Pakistan (Chagai Hills)
Argillic	((float(b3)/b2) le 1.40) and (b4 gt 2600) and ((float(b4)/b6) gt 1.25) and ((float(b5)/b6) le 1.04) and ((float(b7)/b6) ge 1.03)
Phyllic	((float(b3)/b2) le 1.40) and (b4 gt 2600) and ((float(b4)/b6) gt 1.25) and ((float(b5)/b6) gt 1.04) and ((float(b7)/b6) ge 1.05)
	Method 3—southern Iran, southeastern Iran, and southwestern Pakistan
Argillic	((float(b3)/b2) le 1.35) and (b4 gt 2600) and ((float(b4)/b6) gt 1.37) and ((float(b5)/b6)le 1.089) and ((float(b7)/b6) ge 1.03)
Phyllic	((float(b3)/b2) le 1.35) and (b4 gt 2600) and ((float(b4)/b6) gt 1.37) and ((float(b5)/b6)gt 1.089) and ((float(b7)/b6) ge 1.03)

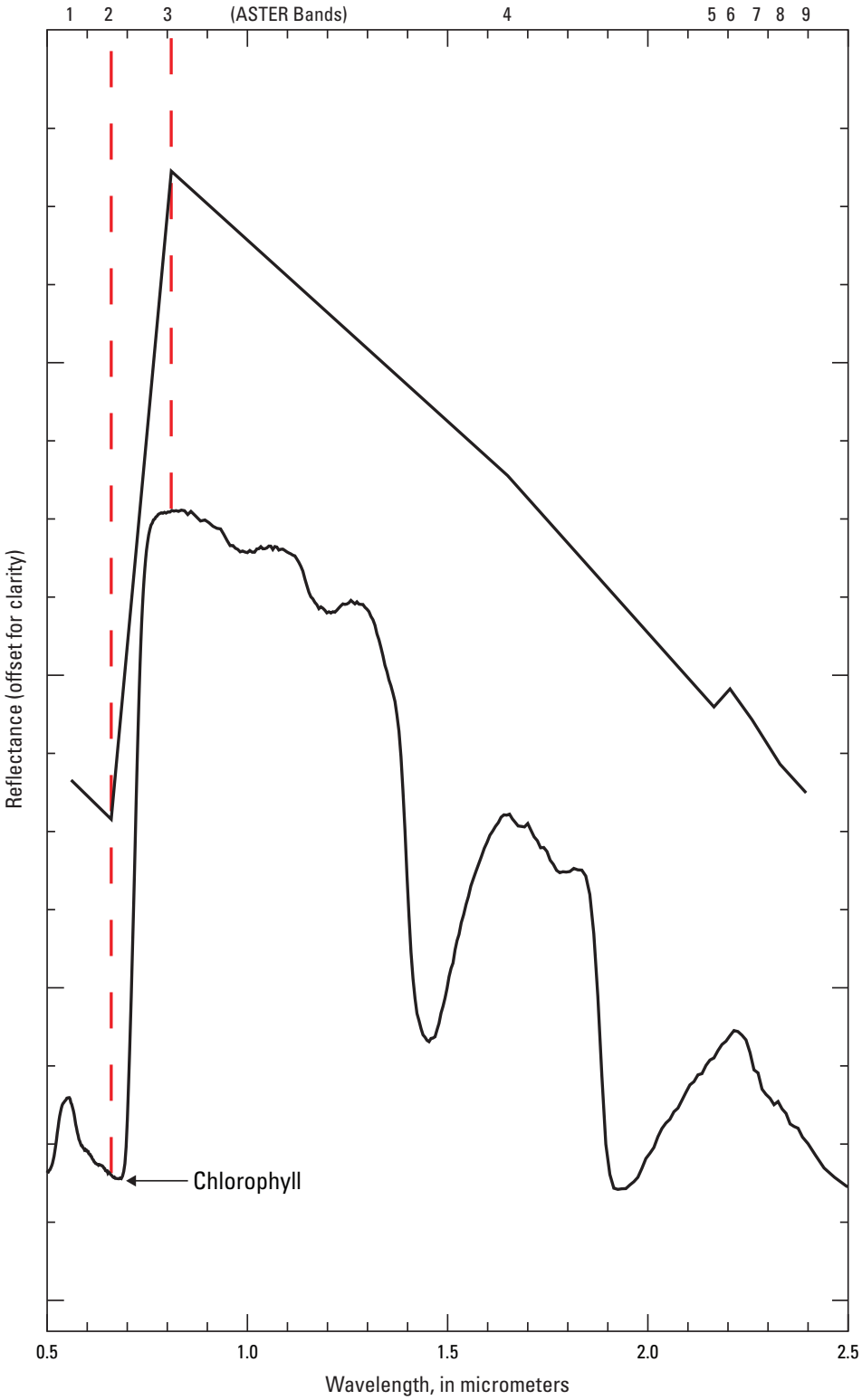

Figure 7. A laboratory spectrum of a green aspen leaf and the same spectrum resampled to Advanced Spaceborne Thermal Emission and Reflection Radiometer (ASTER) bandpasses. ASTER bands 2 and three are highlighted by a red dashed line to emphasize the chlorophyll absorption features at 0.68 micrometers. The ASTER ratio 3/2 is used in the logical operators to mask out green vegetation.

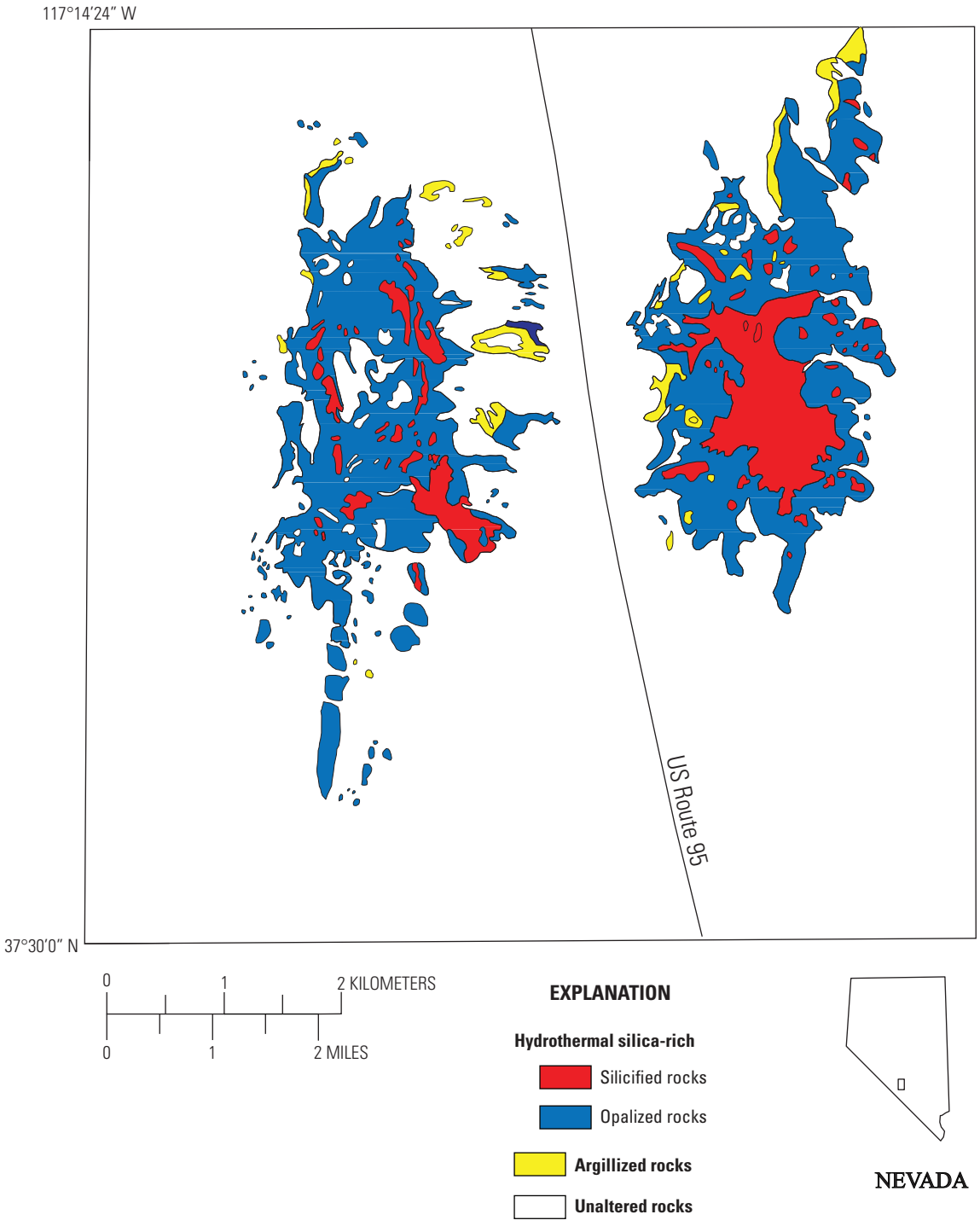

Figure 8. Generalized map showing the distribution of silicified (red map unit), opalized (blue map unit), and argillized (yellow map unit) rocks at Cuprite, Nevada (modified from Ashley and Abrams, 1980); inset map shows location of area in southern Nevada.

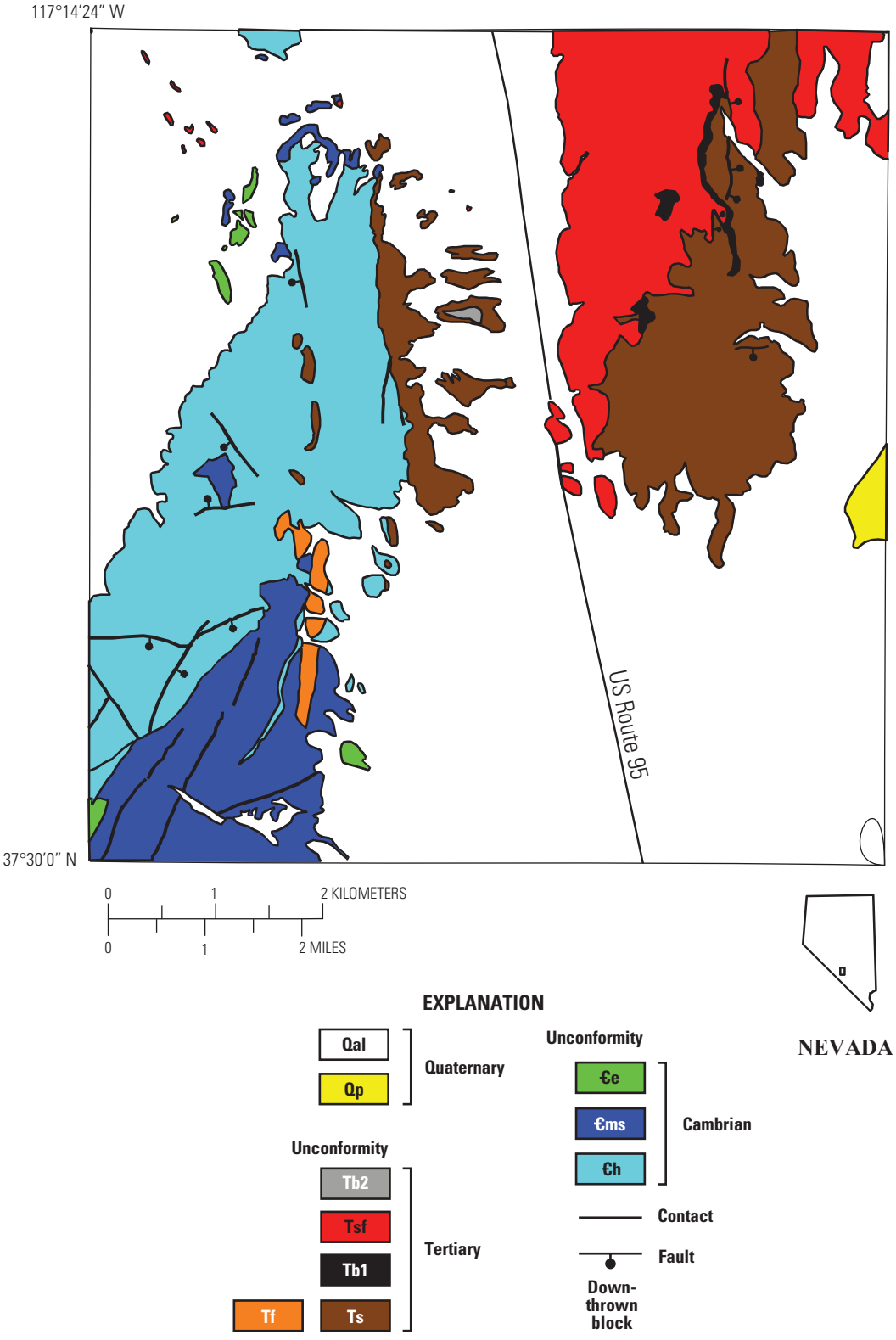

Figure 9. Generalized geologic map of the Cuprite mining district, Nevada. Qal—sand, gravel, and boulders; Qp—playa deposits; Tb2—olivine basalt; Tsf—sodic ash-flow tuff; Tb1—porphyritic olivine basalt; Ts—crystal-rich rhyolite and latite tuff, conglomerate, and sandstone; Tf—quartz latitic felsite; Ꞓe—limestone and chert; Ꞓms—limestone and limey siltstone; Ꞓh—phyllitic siltstone and minor sandy limestone (modified from Ashley and Abrams, 1980; Swayze, 1997); inset map shows location of area in southern Nevada.

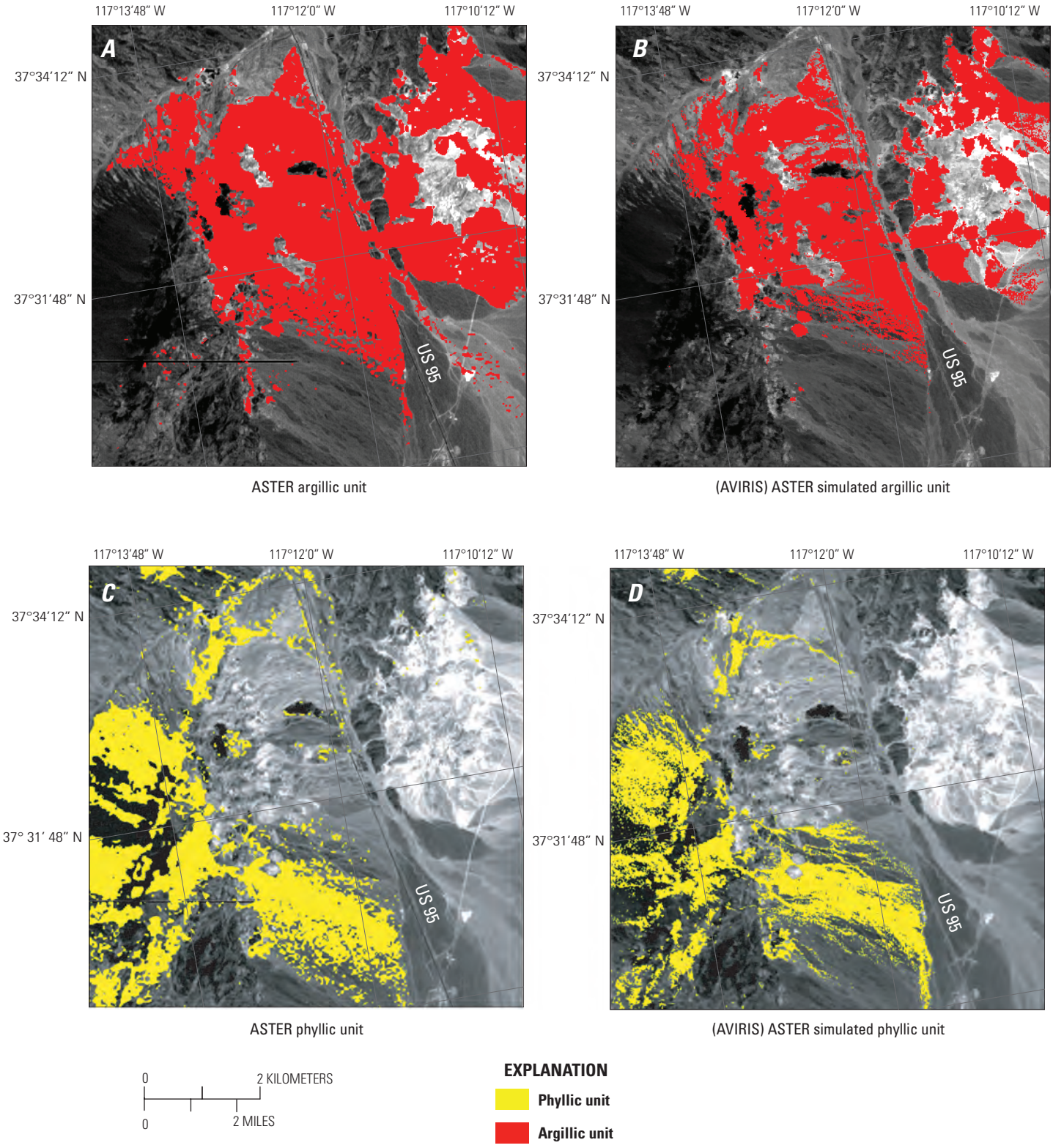

Figure 10. Maps of argillic and phyllic rocks at Cuprite, Nevada, using logical operator algorithms include (*A*) Advanced Spaceborne Thermal Emission and Reflection Radiometer (ASTER) argillic alteration, (*B*) ASTER-simulated (Airborne Visible Infrared Imaging Spectrometer, AVIRIS) argillic alteration, (*C*) ASTER phyllic rocks, and (*D*) ASTER-simulated (AVIRIS) phyllic rocks. Phyllic and argillic units are superimposed on ASTER and ASTER-simulated band 3 images. ASTER argillic and phyllic maps compiled from ASTER reflectance data calibrated to reflectance using calibration method 1 (from Mars and Rowan, 2006).

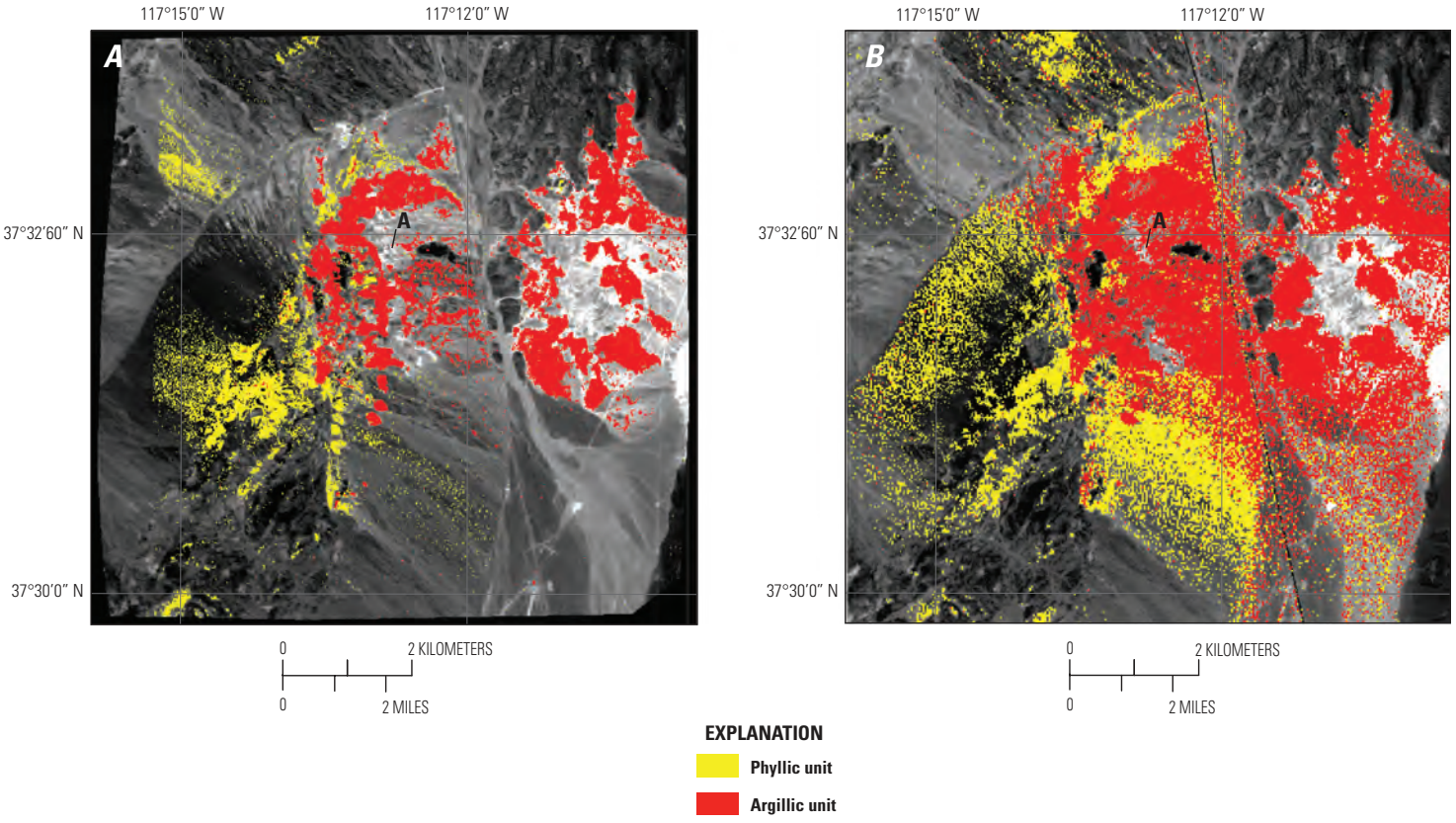

Figure 11. Images of Airborne Visible Infrared Imaging Spectrometer (AVIRIS) and Advanced Spaceborne Thermal Emission and Reflection Radiometer (ASTER) mapped alteration at Cuprite, Nevada. *A,* AVIRIS mapped phyllic- and argillic-altered rocks using matched filtering algorithm. The background image is AVIRIS data convolved to ASTER band 3 (modified from Rowan and others, 2003). *B,* ASTER mapped phyllic- and argillic-altered rocks using logical operators on ASTER data calibrated to reflectance using calibration method 3. The background image is ASTER band 3. Photograph and sample spectra were taken at location "A" and are shown in figure 12. Location "A" is an area where argillic alteration was mapped using ASTER data and logical operators (figure 10*A*) and argillic alteration was not mapped in the same area (figure 10*B*) using AVIRIS data and matched filtering.

The first validation method used LO algorithms and ASTER data calibrated using calibration method 1. The validation method involved a quantitative comparison of ASTER-derived argillic and phyllic maps to similar maps compiled from an ASTER-simulated AVIRIS dataset that was resampled to ASTER VNIR_SWIR bandpasses (fig. 10; Mars and Rowan, 2006). The AVIRIS-ASTER-simulated data were coregistered to the ASTER dataset in order to quantitatively assess alteration mapping accuracy. Each LO compiled mineral map consists of 0 and 1 values; thus, each mineral map could be used as a mask and was quantitatively compared using band math analysis. Band math analysis involves the addition, subtraction, multiplication, or division of the pixel values of images with the same spatial dimensions (ITT, 2008). Mineral maps of the same mineral compiled from the ASTER (**Ad**) and AVIRIS-ASTER simulated data (**AAsd**) were multiplied to produce a map showing the mineral mapped in the same area for both mineral maps (**SA**). The map illustrating the same mineral mapped area (**SA**) was multiplied by the AVIRIS-ASTER compiled mineral map to show areas not mapped as a mineral in the ASTER mineral map but were mapped as a mineral in the AVIRIS-ASTER compiled mineral map (**NMAAsd**). The map illustrating the same mineral mapped area (**SA**) was also multiplied by the ASTER compiled mineral map to show the additional areas mapped in the ASTER mineral map but not mapped in the AVIRIS-ASTER mineral map (**NMAd**).

Band math equations used to quantitatively validate ASTER mineral maps:

SA × **AAsd** = **NMAAsd** (AVIRIS-ASTER mineral mapped area not shown in the ASTER mineral map)

SA × **Ad** = **NMAd** (ASTER mineral mapped area not shown in the AVIRIS-ASTER mineral map)

AAsd—AVIRIS-ASTER-simulated data mineral map (argillic or phyllic)

Ad—ASTER-data mineral map (argillic or phyllic)

SA—same mineral mapped area in **AAsd** and **Ad**

AAsd × **Ad** = **SA** (same mineral mapped area in **AAsd** and **Ad**)

The validation results show that argillic and phyllic patterns are very similar to AVIRIS mapped argillic and phyllic alteration, although there is more ASTER hydrothermal alteration than shown in the AVIRIS-ASTER compiled data (figs. 10 and 11; Mars and Rowan, 2006). For validation method 1, 95 percent of the argillic alteration and 72 percent of the phyllic rocks mapped in the simulated ASTER-AVIRIS dataset were mapped in the ASTER calibrated reflectance datasets (fig. 10). The argillic and phyllic algorithms tend to map up to approximately 40 to 55 percent more altered rock than mapped in the ASTER-AVIRIS simulated data. The overestimation of altered rocks reflects the more noisy characteristics and larger spatial resolution (30 m) of ASTER data compared to the high signal to noise, 18-m spatial resolution AVIRIS data (Yamaguchi and others, 2001; Green and others, 1998; Clark and Swayze, 1996).

A second, more qualitative validation method was used to assess argillic and phyllic alteration maps compiled by using LO algorithms and ASTER data calibrated using calibration methods 2 and 3 (fig. 11). The validation method involved visual comparisons of mineral maps compiled from the full spectral and spatial resolution AVIRIS data to ASTER compiled argillic and phyllic mineral maps. The AVIRIS mineral map was compiled from the results of a previous study of Cuprite, Nevada, where minerals were mapped using AVIRIS reflectance data and a matched filtering algorithm and then grouped and displayed as argillic or phyllic mineral groups (fig 11; Rowan and others, 2003). The qualitative method shows similar patterns of hydrothermal alteration; however, more argillic- and phyllic-altered rocks were mapped using the ASTER data and LO algorithms than were mapped using the matched-filtered AVIRIS data. Suspect areas where phyllic and argillic rocks were mapped using ASTER data, but not mapped in previous studies using AVIRIS data, were spectrally assessed for absorption features to further assess the accuracy of the algorithms (fig. 11). The image spectra of the suspect areas mapped as phyllic or argillic alteration in the ASTER data contain 2.20- and 2.165-µm absorption features, which suggest they are muscovite and kaolinite-alunite mixed spectra. In addition, field investigations of the Cuprite area show that most of the suspect areas mapped using ASTER data are large alluvial fans covered by argillic and phyllic rock fragments. An average field spectrum of seven randomly collected rock fragments from one of the suspect areas that was mapped as argillic alteration exhibits strong 2.165- and 2.2-µm absorption features (figs. 11 and 12). Thus, the overestimation of altered rocks in the second qualitative validation method reflects the inclusion of altered talus in the ASTER argillic and phyllic mineral maps, whereas mapping algorithms in AVIRIS previous studies focused on distinguishing argillic- and phyllic-altered outcrops.

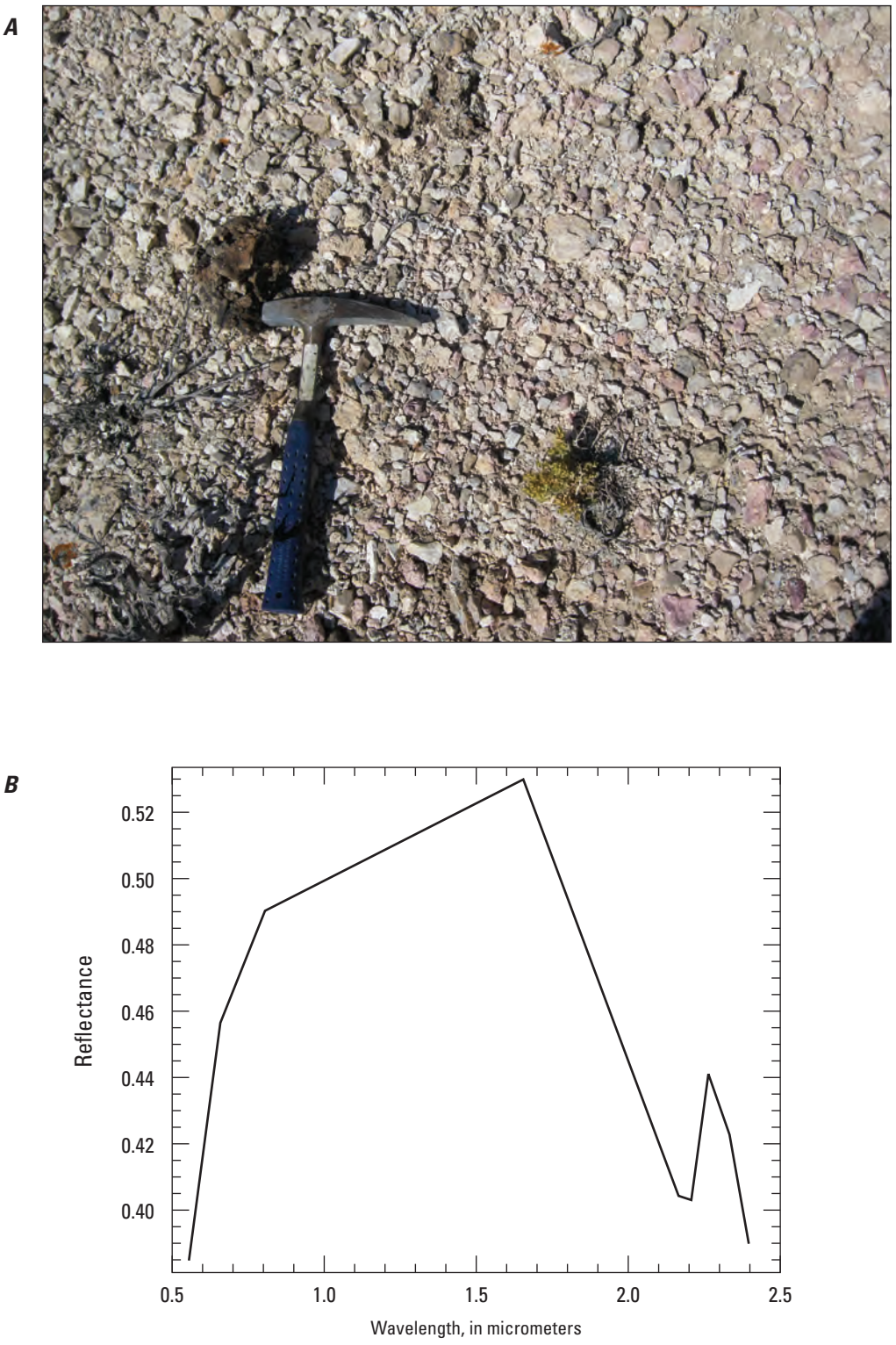

Figure 12. Photograph and average spectrum of argillic-altered rocks that contain alunite and kaolinite at the Cuprite, Nevada, site. *A*, Photograph at location "A" in figure 11. Most of the rock fragments in the photograph consist of alunite and kaolinite. *B*, An average spectrum of seven randomly collected rock fragments from location "A." The average spectrum exhibits intense Al-O-H absorption features at 2.165 and 2.2 micrometers, typical of argillic-altered rocks that contain alunite and kaolinite.

Masking Detrital Clays in Sedimentary Rocks for the Kerman Area, Iran

Detrital clays in sedimentary rocks may be erroneously mapped as hydrothermal alteration clay minerals. Many sedimentary rocks such as mudstone, shale, claystone, and litharenite sandstones contain large amounts of detrital muscovite and clay minerals such as montmorillonite, illite, and kaolinite. In order to mask out detrital clays, an igneous rock mask was produced using two 1:1,000,000-scale Iranian geologic maps (Huber, 1969a,b). Each map was digitized and geo-registered, and polygon vectors were drawn around igneous rock units. The vectors were then converted to a byte mask, visually compared to the Landsat TM mosaic for registration accuracy, and applied to the ASTER alteration data in an area limited to the Kerman region in Iran. The mask confined alteration mapping to areas underlain by igneous rocks in the area covering scenes calibrated using method 1 (plate 1). In contrast, the areas mapped by ASTER data using calibration methods 2 and 3 were based on a geographic information system (GIS) system in which a 1:2,500,000-scale geologic map was overlaid on the hydrothermal alteration map in order to identify alteration associated with igneous rocks (Stocklin and Nabavi, 1973).

Identification of Potential Porphyry Copper Sites

Hydrothermal Alteration Patterns and Associated Deposits

Geologic maps indicate extensive 1 to 2 km in diameter intrusions of Eocene to Miocene diorite, quartz diorite, quartz monzonite, and granodiorite porphyry surrounded primarily by Eocene and Oligocene volcanic tuffs throughout the central part of the UDVB (Huber, 1969a; figs. 13 and 14). ASTER-mapped hydrothermal alteration units in the central part of the volcanic belt typically form circular to elliptical patterns, 1 to 5 km in diameter, which are associated with hydrothermally altered Eocene to Miocene igneous intrusive bodies and surrounding tuffs (figs. 13 and 14; plate 4). Documented porphyry copper deposits at Sar Cheshmeh, Meiduk, and Seridune also exhibit elliptical to circular patterns of argillic and phyllic alteration derived from ASTER data in the central part of the study area (figs. 13*B* and 14*B*; plate 4; Barzegar, 2007; Hassanzadeh, 1993; Ranjbar and others, 2004; Tangestani and Moore, 2002). In addition, alteration maps produced for the Sar-Cheshmeh, Meiduk, and Seridune areas in previous studies show good agreement with the ASTER phyllic and argillic alteration maps (Barzegar, 2007; John and others, 2010; Ranjbar and others, 2004; Tangestani, and Moore, 2002). ASTER-derived alteration patterns superimposed on ASTER and Landsat TM imagery and geologic maps also show circular to elliptical patterns of argillic and phyllic hydrothermal alteration centered on deeply eroded volcanoes that contain copper deposits (fig 13*B*; plate 4; Huber, 1969a). Thus, circular to elliptical alteration patterns of argillic and phyllic hydrothermal alteration, and association with altered intrusive bodies and (or) partially to deeply eroded volcanic edifices, suggest a high potential for copper porphyry deposits based on similarities to current hydrothermal alteration models, alteration mapped in previous deposit studies, and deposit locations on geologic maps (John and others, 2010; Lowell and Guilbert, 1970; Ranjbar and others, 2004; Tangestani and Moore, 2002).

Some of the mapped phyllic and argillic alteration forms elongate patterns in the cores of plunging folds (figs. 14 and 15*A*, *B*, and *C*; plate 4). In addition, Landsat TM imagery and ASTER alteration mapping shows intense fracturing and faulting and alteration along the cores of folds (figs. 15*B* and *C*; plate 4). The shape and limited lateral extent of the alteration and confining structure suggest localized, intense fracturing and fluid flow along fold axes and the potential for mineralization. The axial fracture zones also may act as a pathway for magmas. For example, in the eastern part of the CVB, a geologic map and Landsat TM imagery show the Saindak porphyry copper deposit situated in the core of a syncline (fig. 15*A* and *B*; Canadian Government, 1958).

Previous studies and geologic maps show that linear patterns of primarily phyllic- hydrothermally altered fractures, faults, dikes, and sills in the study area are typically associated with polymetallic vein and epithermal deposits (Mars and Rowan, 2006; Grabeljsek and others, 1972; Regard and others, 2004; Valeh, 1972). In the study area, ASTER hydrothermal alteration and geologic maps show linear patterns of phyllic-altered rocks that are associated with fractures and faults and include (1) an extensive phyllic hydrothermally altered fracture-fault zone in an anticline adjacent to the Saindak porphyry copper deposit (fig. 15*A*, *B*, and *C*) and (2) Eocene-Oligocene volcanic rocks that contain phyllic-altered faults and fractures throughout the Zagros-Makran transform zone in the south central and central parts of the UDVB (fig. 3; plates 4 and 9; Mars and Rowan, 2006). In some areas such as Saindak, the altered faults and fractures may be the exterior epithermal part of the adjacent porphyry system (fig. 15*A*, *B*, and *C*).

Altered tuffs also were mapped using ASTER data in the UDVB. The tuffs are typically much more laterally extensive than hydrothermally altered rocks associated with porphyry systems, and when deformed, tend to form elongate, folded and (or) faulted structures (fig. 16*A*, *B*).

The Neogene Baluchistan volcanic arc, which over prints the southeastern part of the UDVB and the CVB, consists primarily of Quaternary andesite and includes at least three large composite volcanoes—Bazman, Taftan, and Koh-i-Soltan (plate 5). The ASTER mineral maps show that all three volcanoes have laterally extensive hydrothermal phyllic and

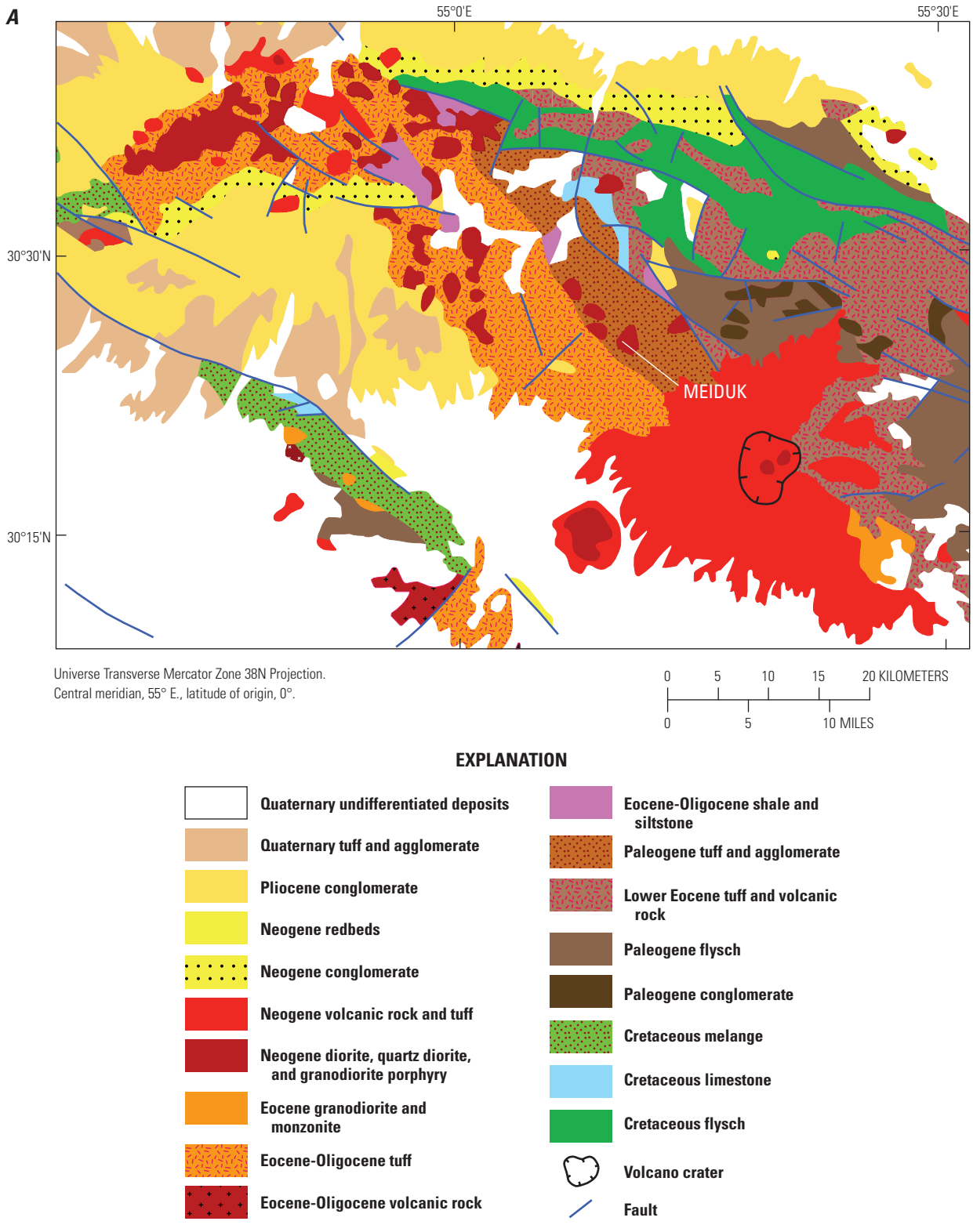

Figure 13. Geology and alteration in the Meiduk Mine area, Iran (see figure 4). *A*, Geologic map (modified from Huber, 1969a). *B*, Landsat TM band 7 image with Advanced Spaceborne Thermal Emission and Reflection Radiometer (ASTER) mapped argillic and phyllic alteration of the area around the Meiduk copper mine, Iran, in the south central part of the study area (plate 4; Modified from Mars and Rowan, 2006).

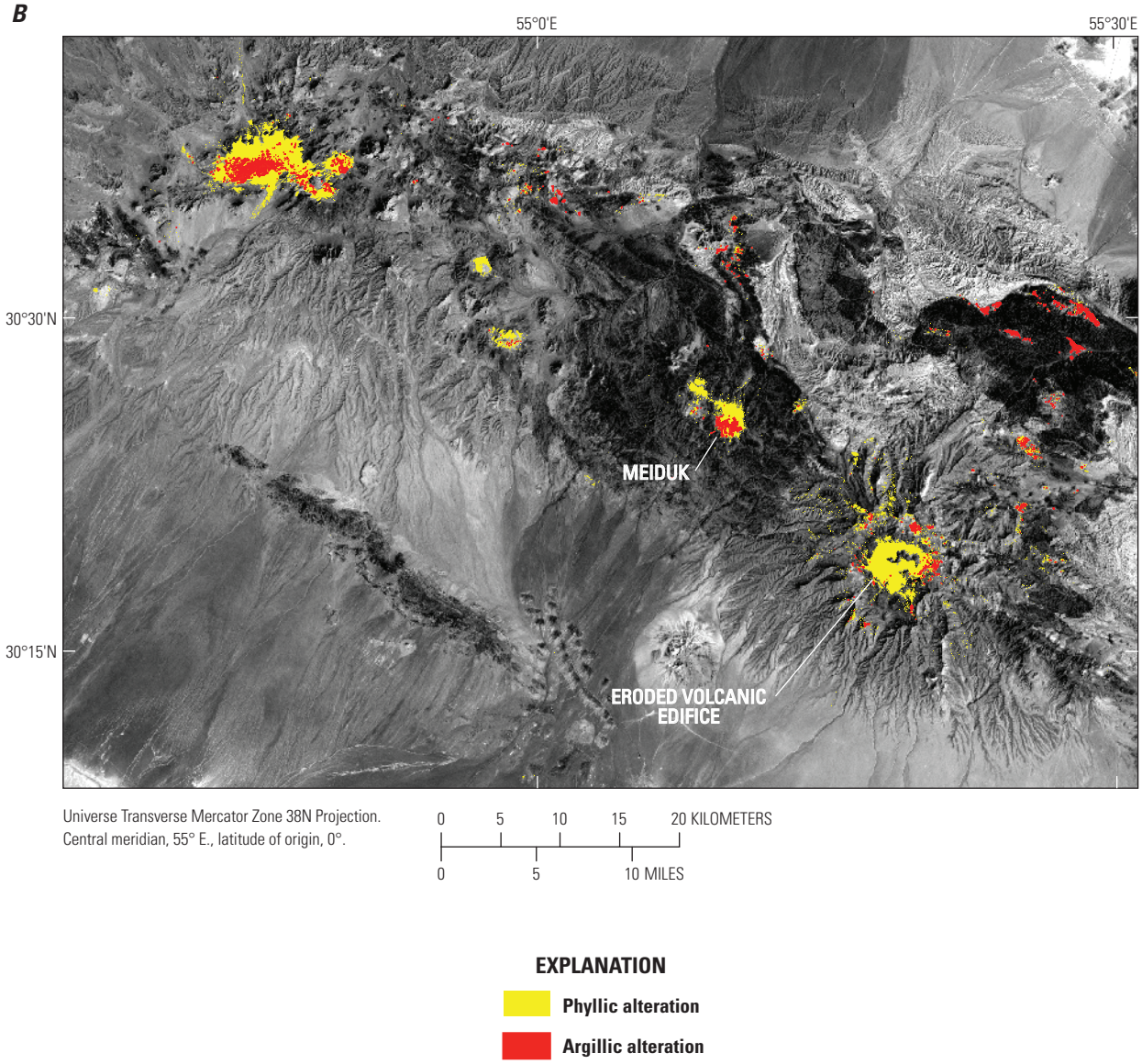

Figure 13.—Continued

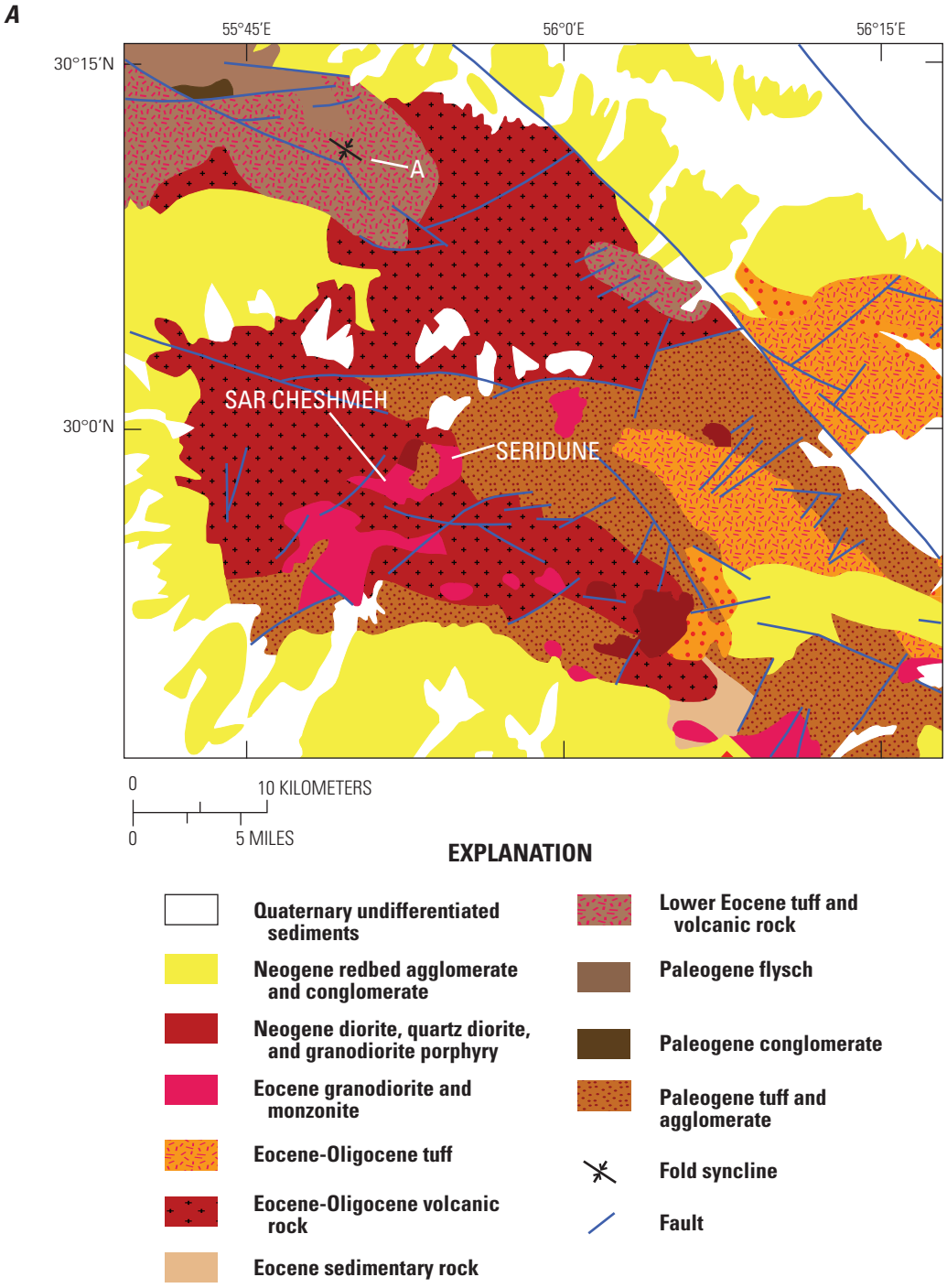

Figure 14. Geology and alteration in the central part of the study area in western Asia. *A*, Geologic map (modified from Huber, 1969a). *B*, Landsat TM band 7 image with argillic and phyllic alteration of the area around the Sar Cheshmeh Copper Mine, and the Seridune porphyry copper deposit, Iran (plate 4; modified from Mars and Rowan, 2006). Location A is the altered core of a fold.

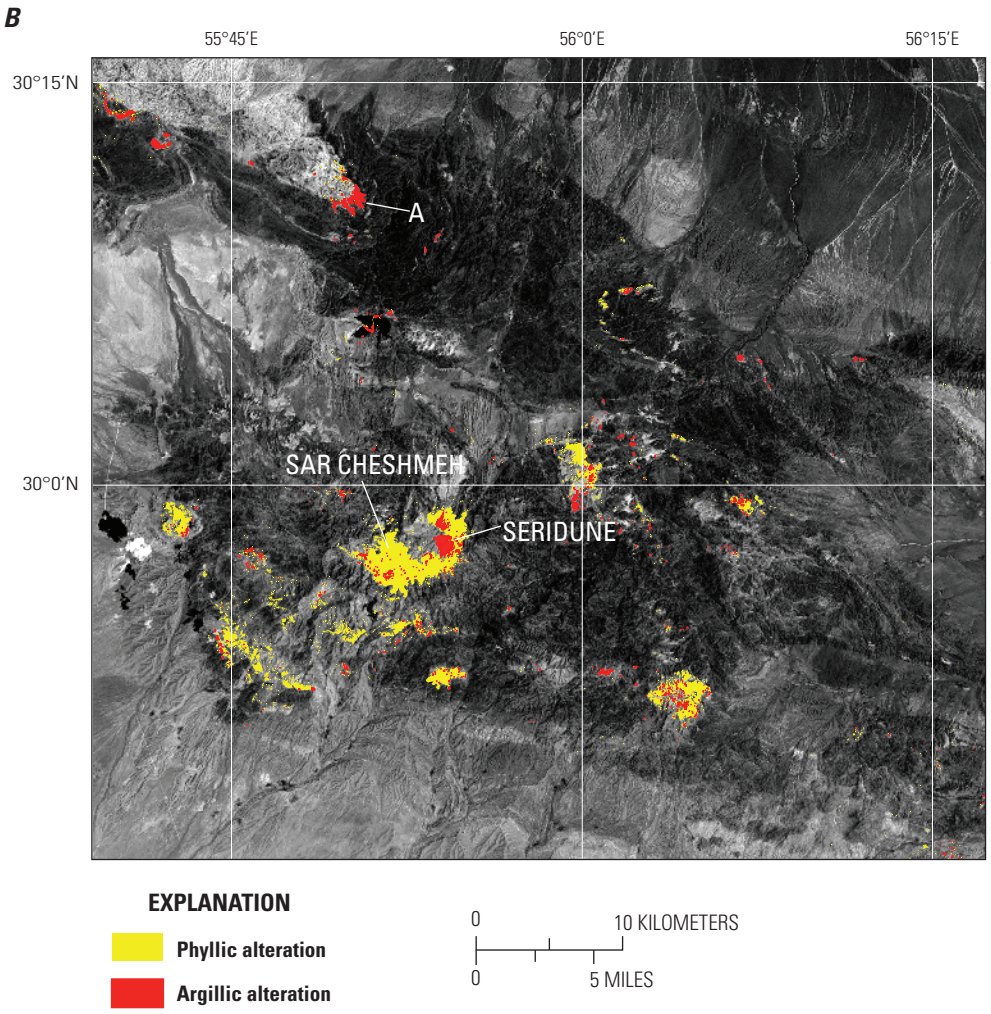

Figure 14.—Continued

argillic alteration on their edifices (plate 5). The hydrothermal alteration on the volcanic edifices is due to recent volcanic and hydrothermal processes that are not associated with porphyry copper deposits. However, Landsat TM and ASTER imagery and an ASTER alteration map show three deeply eroded, hydrothermally altered, volcanic edifices northwest of Taftan (fig. 17*A*, *B*). The three highly eroded volcanoes exhibit circular to elliptical patterns of argillic and phyllic alteration, which are consistent with the same patterns seen at the Seridune porphyry copper deposit (figs. 14*B* and 17*B*, *C)*. Surrounding the eroded volcanic centers are radiating linear patterns of dominantly phyllic-altered rocks (fig. 17*C*). The elliptical patterns of argillic- and phyllic-altered rocks exhibit alteration patterns typical of porphyry copper deposits and the areas of linear alteration may be associated with epithermal deposits (fig. 17*C*).

Potential Porphyry Copper Sites

Potential porphyry copper sites were identified for the UDVB and the CVB in order to prioritize areas of exploration and to assist in estimating the number of previously undiscovered deposits in mineral assessments (plates 7–10). Circular to elliptical patterns of argillic- and phyllic-altered rocks associated with intrusive bodies were considered to have the highest probability of hosting porphyry ore deposits. Assessments, however, typically consider porphyry deposits to a depth of 1 km, and alteration patterns related to porphyry systems may be either structurally deformed or partially concealed by other deposits such as eolian sands. Thus, some potential porphyry sites were selected on the basis of alteration types and patterns that are associated with volcanic rocks and may exhibit more irregular patterns of ASTER-mapped hydrothermally altered rocks.

To provide a description based on physical characteristics of each potential porphyry copper site, the ASTER alteration map, a tectonic map, a copper deposits map, and a deposit database were used to record physical properties of each site in an ArcGIS database for each site (Bazin and Hubner, 1969; Singer and others, 2008; Stocklin and Nabavi, 1973). Physical properties include alteration type, surficial alteration pattern density, country rock type, alteration pattern shape, associated land forms, size, existing deposits or occurrences, and the presence or absence of “bleached” (light colored) surrounding rocks in the Landsat false color composite (R=7, G=4, B=2) mosaic (appendix B; NASA, 2003).

Urumieh-Dokhtar Volcanic Belt

Using the ASTER hydrothermal alteration map, 178 potential porphyry copper targets were identified in the UDVB (plates 7–10; appendix B). The Sar Cheshmeh and Meiduk mines are the largest porphyry copper deposits in the region (Singer and others, 2008). GIS analysis shows that 31 of the 178 potential targets, including the mine at Sar Cheshmeh, consist of large (greater than 5 km), circular to elliptical, dense patterns of argillic- and phyllic-altered volcanic and igneous intrusive rocks in the volcanic belt (appendix B). In addition, GIS analysis indicates that 36 sites, including the Meiduk Mine, consist of small (less than 5 km), circular to elliptical, dense patterns of argillic- and phyllic-altered volcanic and igneous intrusive rocks (appendix B). The copper deposit map and copper database indicated that four of the potential deposit sites that have characteristics similar to those at the Sar Cheshmeh and Meiduk mines contain known economic deposits, and 16 potential sites have known copper occurrences (appendix B; Bazin and Hubner, 1969; Singer and others, 2008). The southern part of the UDVB west of the Makran transform zone contains the highest density of altered intrusive rocks with circular to elliptical patterns of argillic and phyllic hydrothermal alteration (plate 4).

Chagai Volcanic Belt

Using the ASTER hydrothermal alteration map, 23 potential porphyry copper sites based on alteration types and patterns were identified in the CVB (plate 10; table 1). GIS analysis indicates that seven sites, including Reko Diq (a known deposit), consist of large (greater than 5 km), circular to elliptical, dense patterns of argillic- and phyllic-altered volcanic and igneous intrusive rocks that are similar in alteration characteristics to Sar Cheshmeh (appendix B). A total of five sites consist of small (less than 5 km) circular to elliptical, dense patterns of argillic- and phyllic-altered volcanic and igneous intrusive rocks, which are similar to alteration characteristics found at the Meiduk deposit (appendix B). The physical characteristics of known deposits at Saindak and Reko Diq consist of circular, small to large patterns of phyllic-altered rocks. The contrast in alteration patterns of Saindak and Reko Diq to other known deposits such as Sar Cheshmeh may be due to partial burial of the deposits by sands, as indicated by ASTER and Landsat TM images (NASA, 2003; Tucker and others, 2004; Rowan and others, 2006).

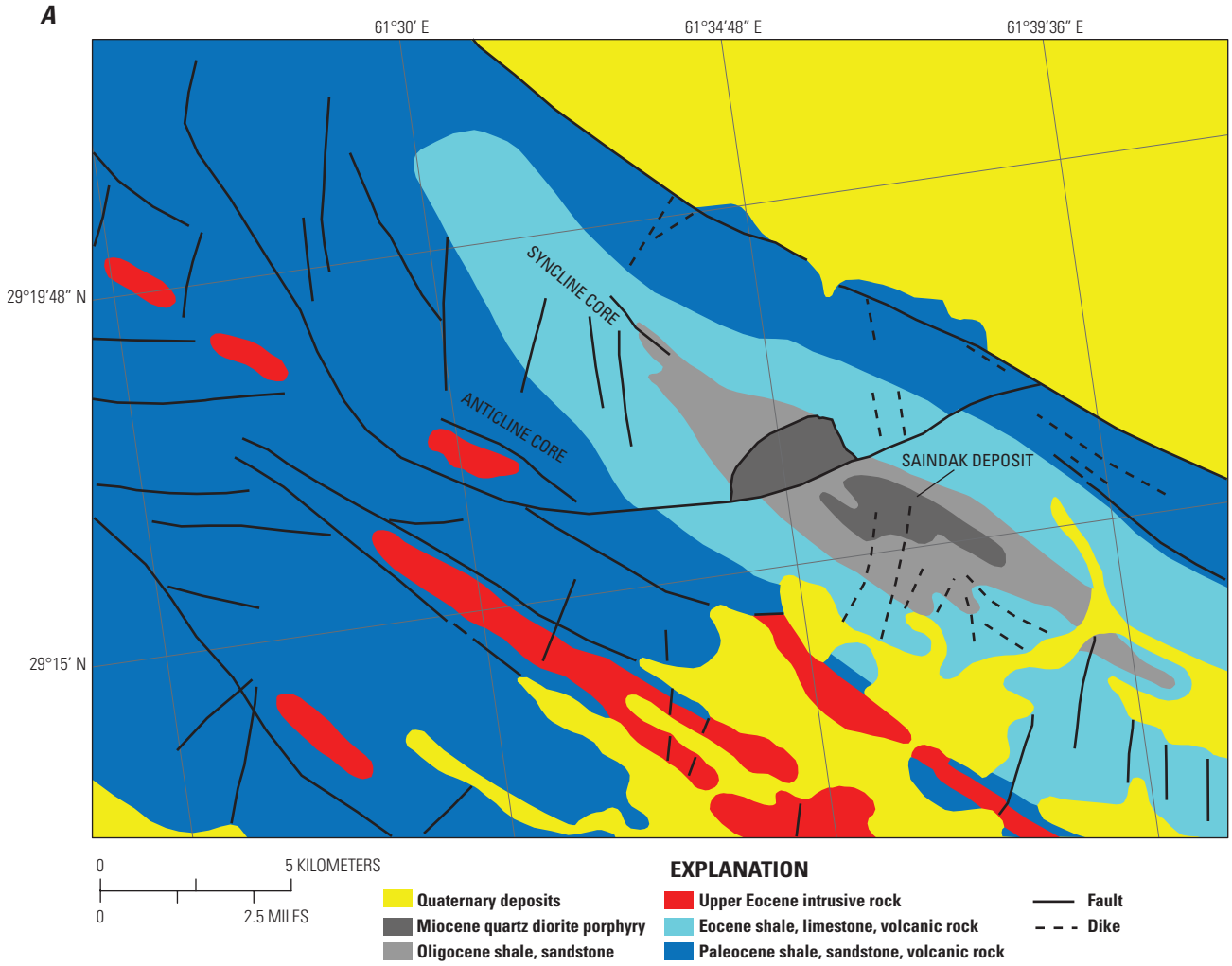

Figure 15. Geology and alteration at the Saindak porphyry deposit (see figure 4). *A*, Geologic map (modified from Canadian Government, 1958). *B*, Landsat TM false color composite (R=7, G=4, B=2). *C*, Advanced Spaceborne Thermal Emission and Reflection Radiometer (ASTER) phyllic and argillic alteration overlaid on a Landsat TM band 7.

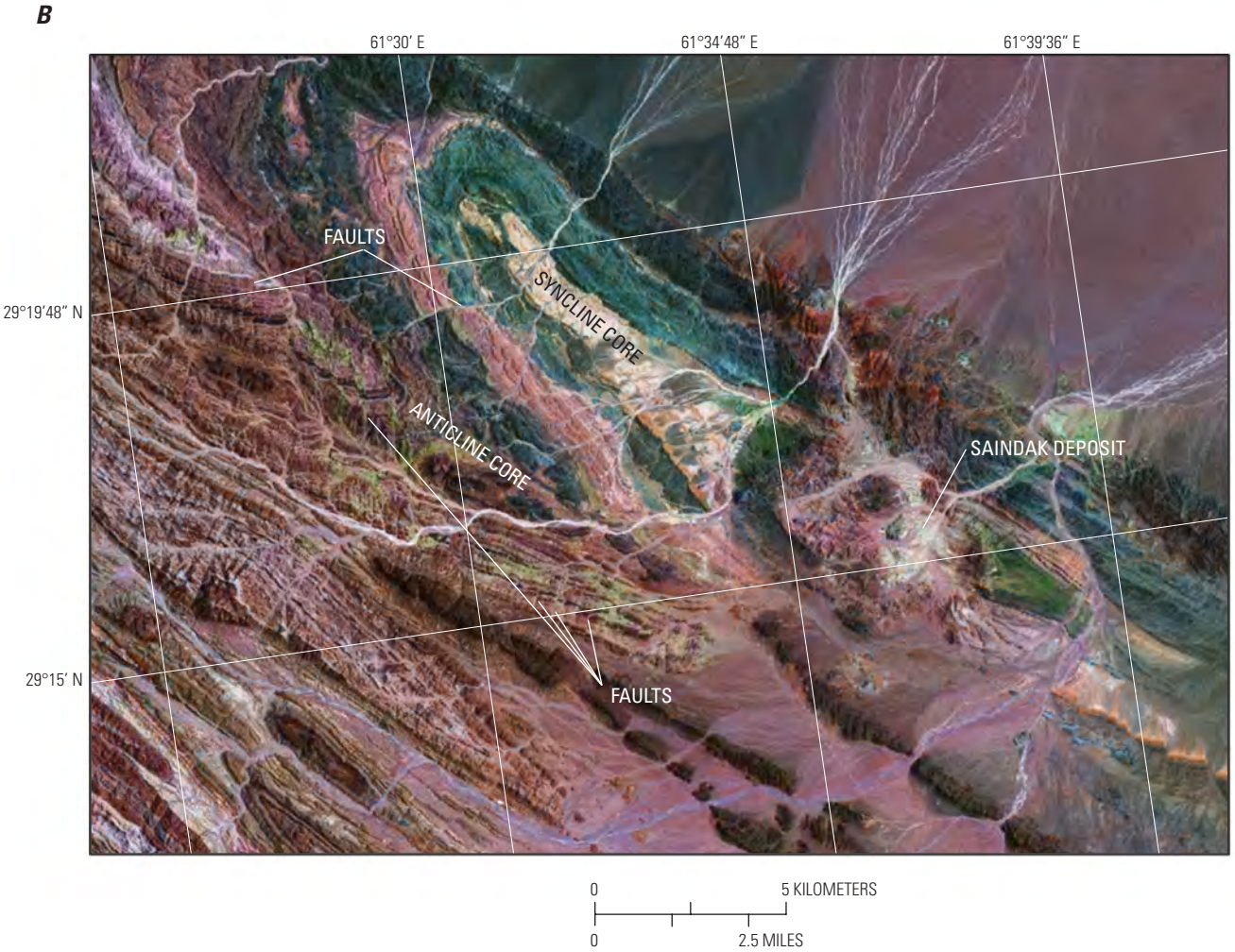

Figure 15.—Continued

c

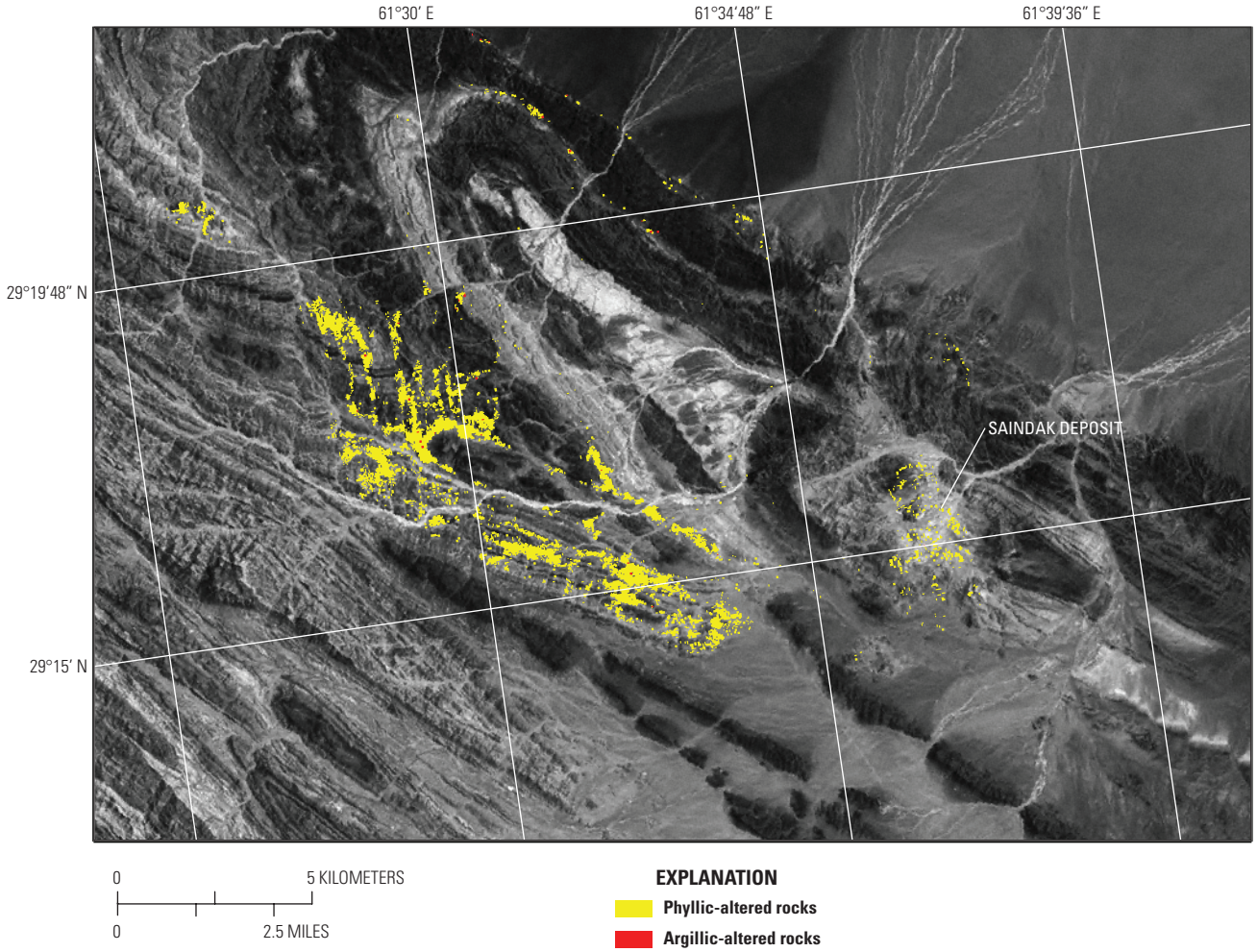

Figure 15.—Continued

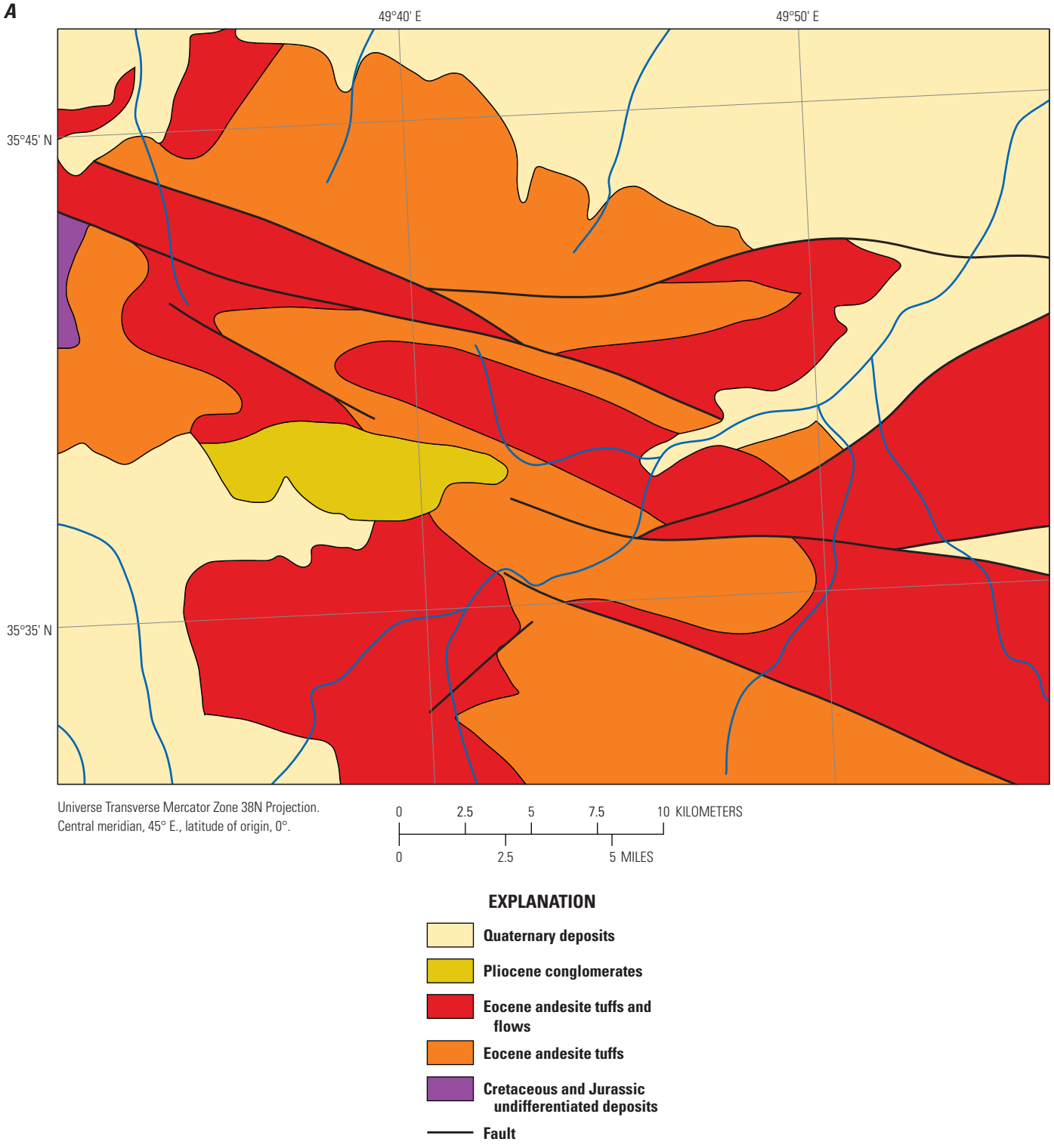

Figure 16. Geology and alteration in the northwestern part of the study area in western Asia. *A*, Geologic map (modified from Huber, 1969b). *B*, Advanced Spaceborne Thermal Emission and Reflection Radiometer (ASTER) phyllic and argillic alteration overlaid on a Landsat TM band 7 of altered tuff deposits.

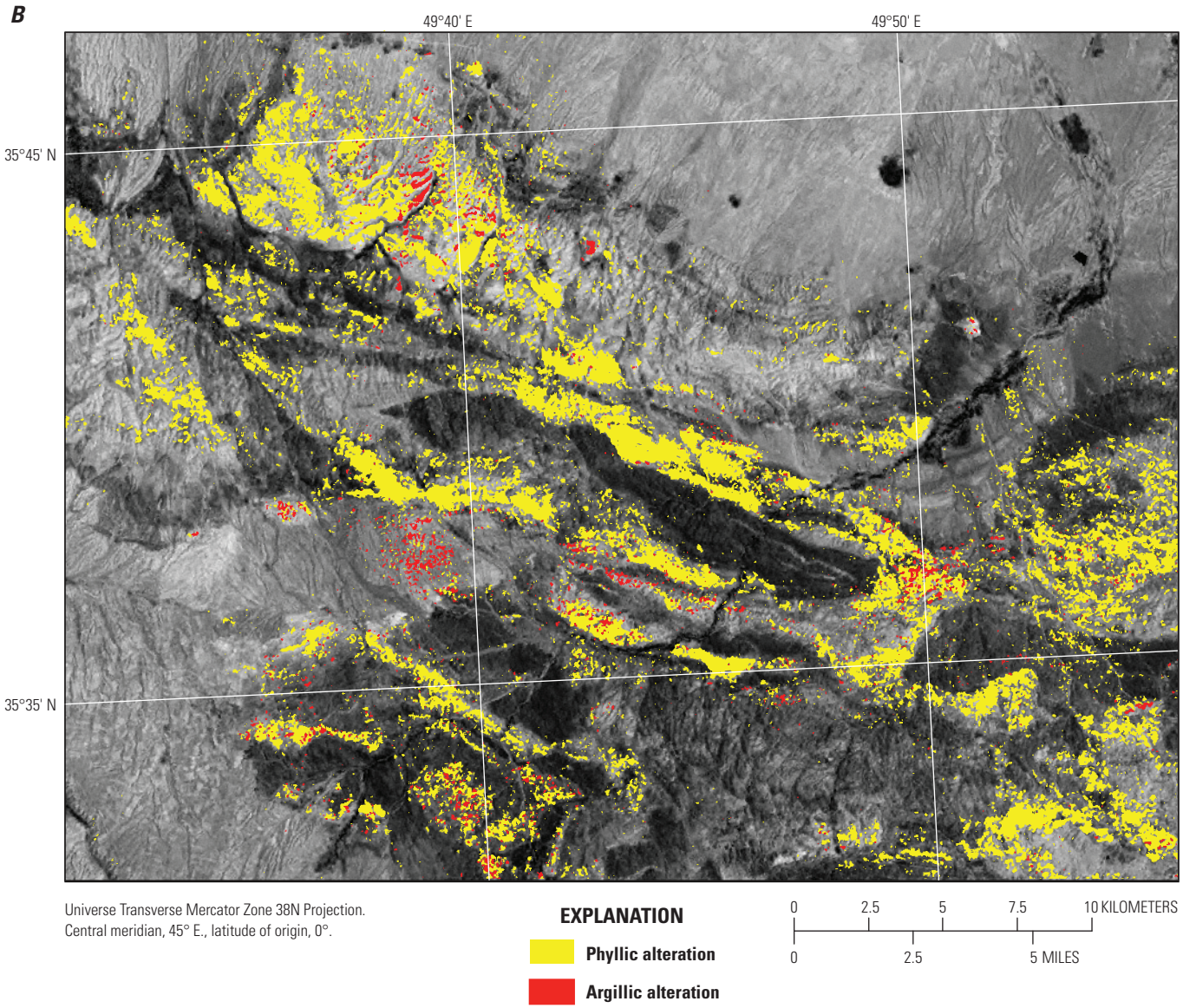

Figure 16.—Continued

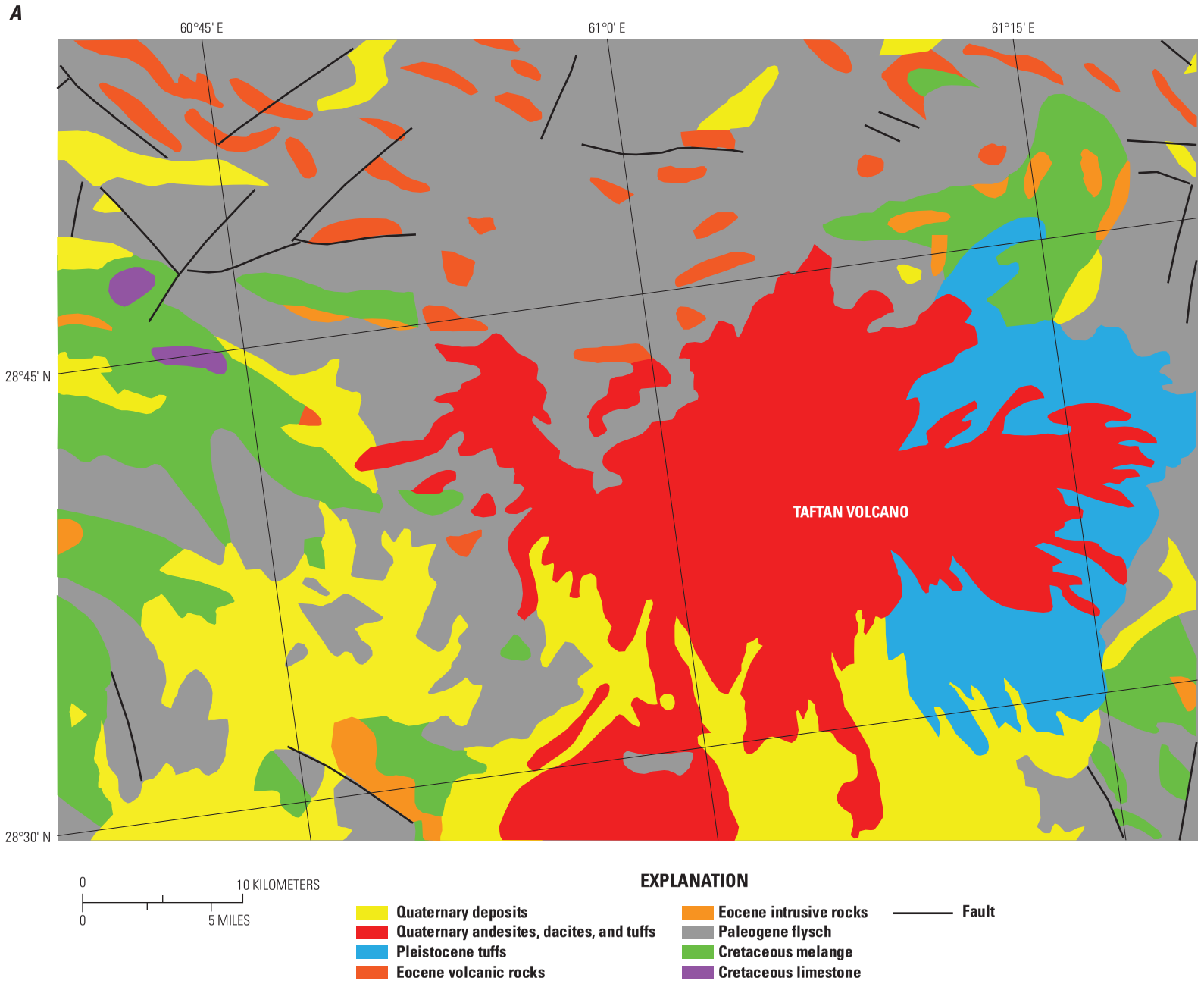

Figure 17. Geology and alteration of the Taftan Volcano, Iran, and surrounding area. *A*, Geologic map (Modified from Huber, 1969b). *B*, Landsat TM false color composite (R=7, G=4, B=2). *C*, Advanced Spaceborne Thermal Emission and Reflection Radiometer (ASTER) phyllic and argillic alteration overlaid Map of potential porphyry copper sites and ASTER hydrothermal alteration in the south central part of the Urumieh-Dokhtar volcanic belt in south central Iran. Alteration units include argillic- and phyllic-altered rocks (red and yellow, respectively) mapped using ASTER data. The background is an orthorectified Landsat TM band 7 grayscale image.

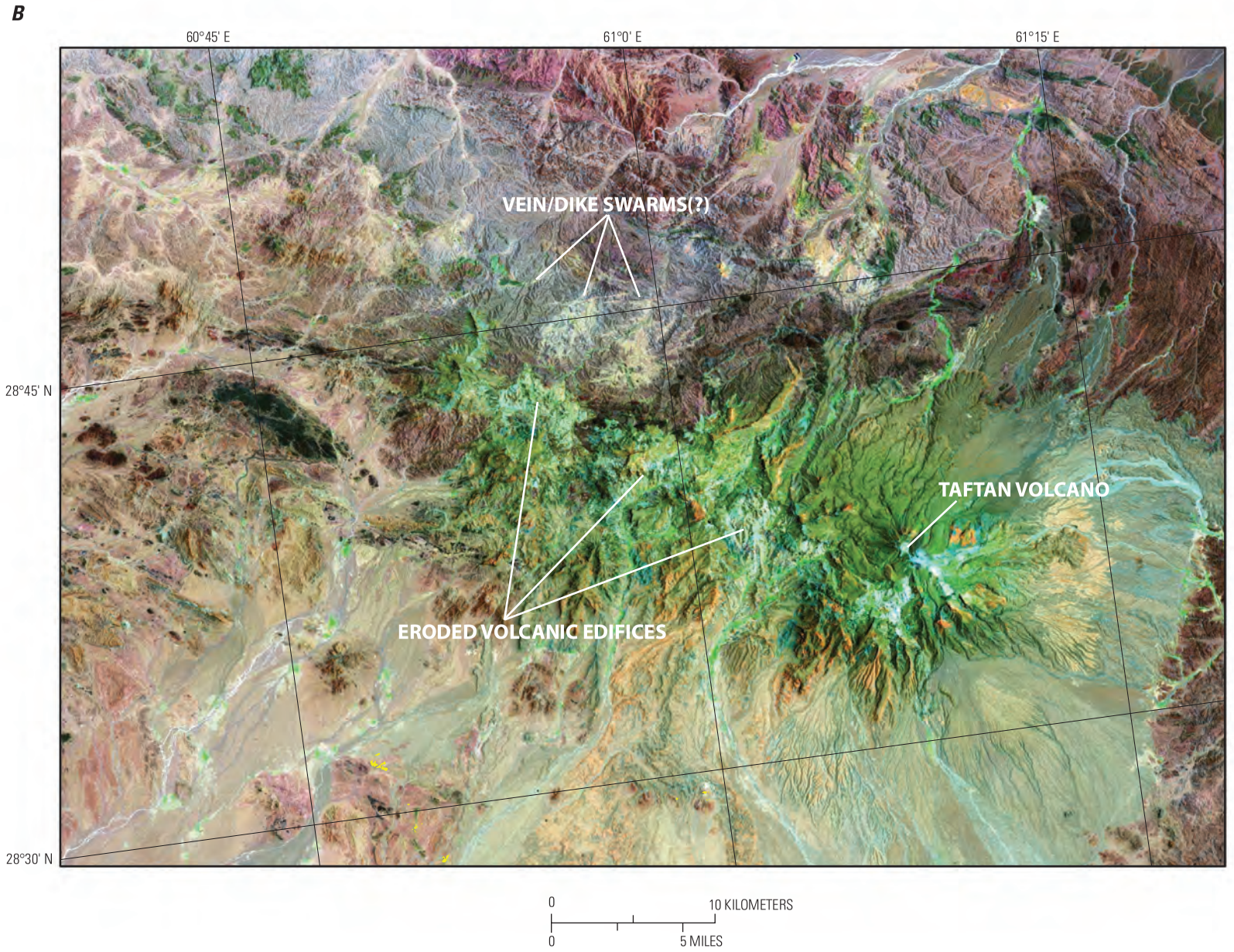

Figure 17.—Continued

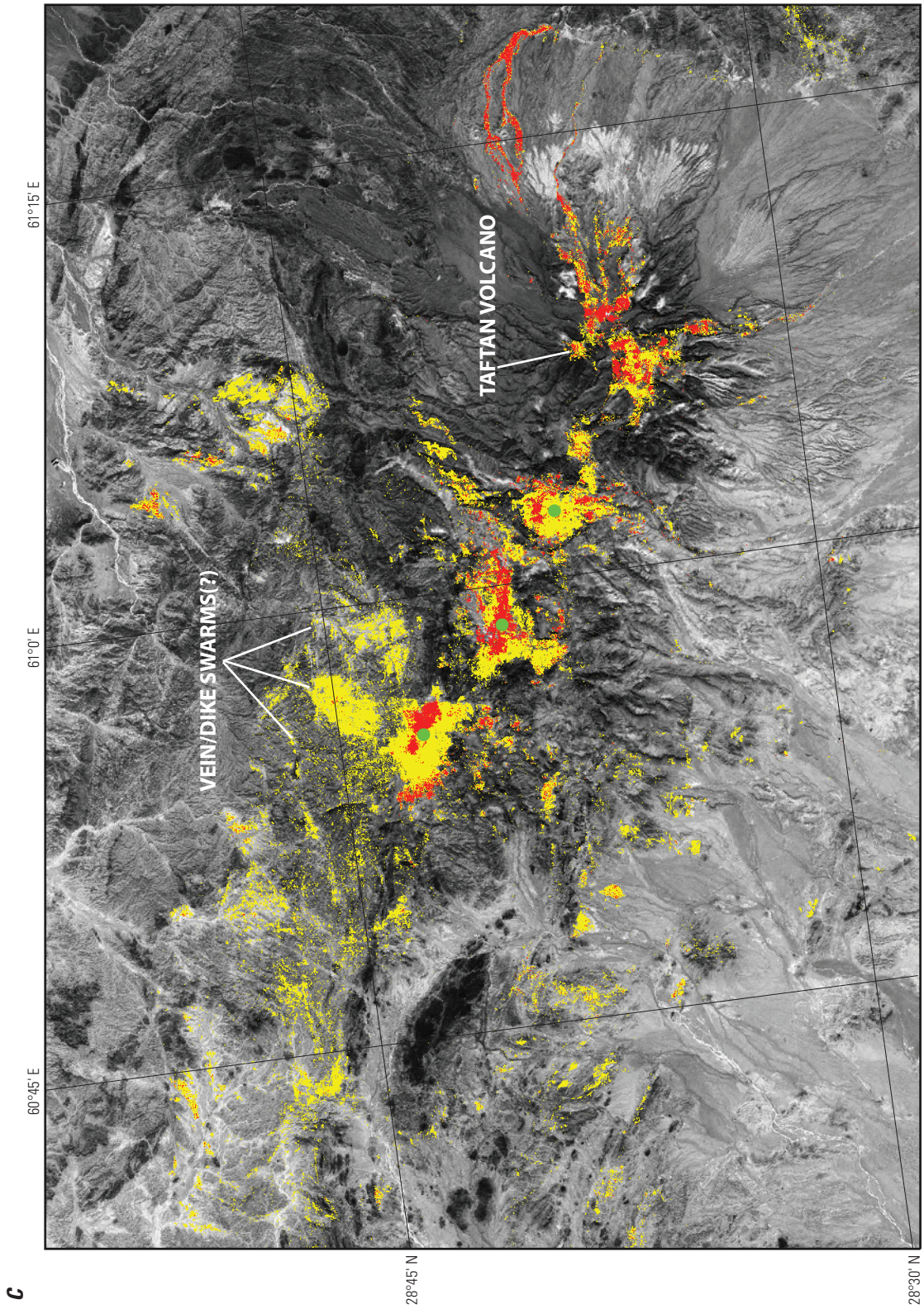

Figure 17.—Continued

Summary and Conclusions

LO algorithms can be used to effectively map argillic and phyllic alteration, provided the ASTER data are accurately calibrated. Calibration methods included (1) using Hyperion data to calibrate AST_07 ASTER reflectance data, (2) converting ASTER Level_1b radiance data to reflectance data using MODIS water vapor data and atmospheric removal software and correcting the ASTER reflectance data using Hyperion data, and (3) correcting ASTER Level_1b radiance data using crosstalk correction software and radiance correction factors and converting the ASTER Level_1b data to reflectance using MODIS water vapor data and atmospheric removal software. LO algorithms apply multiple band ratios and band thresholds to mask green vegetation, low-reflectance, or noisy pixels, and used ratios of ASTER bands 4, 5, 6, and 7 to resolve absorption features in the 2.17- to 2.20-µm region related to argillic- and phyllic-altered rocks. The calibration and LO mapping technique was tested at Cuprite, Nevada, using spectral data collected from field samples, mineral maps from previous studies, an AVIRIS dataset resampled to ASTER bandpasses, and a calibrated ASTER reflectance dataset. The argillic and phyllic spectral units mapped by the argillic and phyllic LOs are similar in shape to phyllic and argillic mineralogy in maps from previous studies. Ninety-five percent of the argillic alteration mapped in the simulated AVIRIS-ASTER dataset was mapped in the ASTER reflectance datasets. Seventy-two percent of the phyllic rocks mapped using the simulated AVIRIS-ASTER dataset were mapped using the AST_07 reflectance dataset. Spectroscopic examination of erroneously mapped argillic (47 percent) and phyllic (56 percent) areas indicate that the error is most likely due to differences in signal to noise and spatial resolution variations between the AVIRIS and ASTER instruments.

Argillic and phyllic alteration maps were compiled for the UDVB, CVB, and AMB using calibrated ASTER reflectance data and LO algorithms. Argillic and phyllic spectral units indicate distinctive patterns of hydrothermal alteration that can be attributed to faults, fractures, and intrusive rocks. In the central part of the UDVB and at the Sain Dak porphyry deposit in Pakistan, primarily phyllic alteration forms linear patterns that are associated with faults and other linear features. The central part of the study area contains numerous 1- to 5-km circular to elliptical patterns of mapped phyllic and argillic alteration. These hydrothermally altered rocks are associated with Eocene to Miocene intrusive igneous rocks and, in some areas such as Meiduk and Sar Cheshmeh, host mined porphyry copper deposits. The Baluchistan volcanic arc contains mostly andesitic and basaltic rocks that are not hydrothermally altered except for the summits of recent, large composite volcanoes such as Bazman, Taftan, and Koh-I-Sultan and areas surrounding Taftan Volcano.

Potential sites for porphyry copper-type mineralization were selected to assist in exploration and assessments of undiscovered porphyry copper deposits. The potential porphyry copper sites were defined using a geologic map, a copper deposits location map, and the ASTER argillic-phyllic hydrothermal alteration map compiled for this study. Altered intrusive bodies forming circular to elliptical patterns of hydrothermal alteration that were similar to known deposits such as Sar Cheshmeh and Meiduk in size, alteration patterns, types, and density were selected as potential porphyry copper sites. Because some intrusive porphyries may be concealed by overlying volcanic rocks or may have been deformed by tectonic processes, additional potential porphyry copper sites were selected that contained altered volcanic rocks and exhibited more irregular patterns of altered rocks. As a result, 178 potential porphyry copper sites were defined along the UDVB, and 23 sites were defined along the CVB. Thus, the ASTER argillic and phyllic hydrothermal alteration map illustrates regional hydrothermal alteration and can help identify potential porphyry copper sites.

Acknowledgments

U.S. Geological Survey colleagues Todd Hoefen and Bernard Hubbard provided helpful technical reviews of the report. Connie Dicken compiled the GIS and prepared the metadata, and Pamela Cossette reviewed the GIS. Michael DeMarr prepared figures and plates. Heather Parks, Niki Wintzer, and Shyla Hatch edited figures and plates. The application of ASTER data to mineral exploration and assessment would not be possible without the pioneering work of our deeply missed colleague Larry Rowan.

References Cited

Abrams, M.J., Brown, D., Lepley, L., and Sadowski, R., 1983, Remote sensing of porphyry copper deposits in southern Arizona: Economic Geology., v. 78, no. 4, p. 591–604.

Abrams, M.J., and Brown, D., 1984, Silver Bell, Arizona, porphyry copper test site report, *in* the Joint NASA/Geosat Test Case Project Final Report: Tulsa, Oklahoma, The American Association of Petroleum Geologists, chapter 4, p. 4-1–4-73.

Alavi, M., and Hushmandazdeh, A., 1976, Geological map of the Torud quadrangle: Tehran, Geological Survey of Iran, scale 1:250,000.

Amidi, S.M., 1984, Geological map of the Saveh quadrangle: Tehran, Geological Survey of Iran, scale 1:250,000.

Ashley, R.P., and Abrams, M.J., 1980, Alteration mapping using multispectral images—Cuprite mining district, Esmeralda County, Nevada: U.S. Geological Survey Open-File Report 80–367, 17 p.

Barzegar, H., 2007, Geology, petrology and geochemical characteristics of alteration zones within the Seridune prospect, Kerman, Iran, [unpublished Ph.D. dissertation]: Geo resources and material technology of the Rheinisch Westfäli Technical University Aachen, Aachen, Germany, 180 p. (Also available at http://darwin.bth.rwth-aachen.de/opus3/volltexte /2007/2009/pdf/Barzegar_Hassan.pdf.)

Bazin, D., and Hubner, H., 1969, Copper occurrences in Iran: Tehran, Offset Press Incorporated, Geological Survey of Iran, scale 1: 3,000,000.

Biggar, S.F., Thome, K.J., McCorkel, J.T., and D'Amico, J.M., 2005, Vicarious calibration of the ASTER SWIR sensor including crosstalk correction: Proceedings of the International Society Optical Engineering, v. 5882, p. 588217.

Canadian Government, 1958, Reconnaissance geology of part of West Pakistan: Canadian Government, Geological map no. 21, Robat, scale 1:253,440.

Clark, R.N., Swayze, G.A., and Gallagher, A.J., 1993a, Mapping minerals with imaging spectroscopy: U.S. Geological Survey Bulletin 2039–B, p.141–150.

Clark, R.N., Swayze, G.A., Gallagher, A., King, T.V.V., and Calvin, W.M., 1993b, The U.S. Geological Survey, Digital Spectral Library, version 1, 0.2 to 3.0 microns: U.S. Geological Survey Open-File Report 93–592, 1340 p. (Also available at http://speclab.cr.usgs.gov.)

Clark, R.N., and Swayze, G.A., 1996, Evolution in imaging spectroscopy analysis and sensor signal-to-noise—An examination of how far we have come: 6th Annual Jet Propulsion Laboratory (JPL) Airborne Earth Science Workshop March 4–8, JPL, Pasadena, California, p. 49–53. (Also available at http://speclab.cr.usgs.gov/map.intro.html.)

Dimitrijevic, M.D., 1973, Geology of the Kerman region: Tehran, Geological Survey of Iran, report Yu/52.

Fujisada, H., 1995, Design and performance of ASTER instrument: Proceedings of the International Society Optical Engineering, v. 2583, p. 16–25.

Gao, B., and Kaufman, Y.J., 1998, Algorithm technical background document—The MODIS near-IR water vapor algorithm, product ID MOD05, total precipitable water: Science Publications and Reports, v. 25. (Also available at http://modis.gsfc.nasa.gov/data/atbd/atbd_mod03.pdf.)

Grabeljsek, V., Cvetic, S., and Dimitrijevic, M.N, 1972, Geological map of Iran, sheet 7547—Sabzevaran: Tehran, Offset Press Incorporated, Geological Survey of Iran, scale 1:100,000.

Green, R.O., Eastwood, M.L., Sarture, C.M., Chrien, T.G., Aronsson, M., Chippendale, B.J., Faust, J. A., Pavri, B.E., Chovit, C.J., and Solis, M., 1998, Imaging spectroscopy and the airborne visible/infrared imaging spectrometer (AVIRIS): Remote Sensing of Environment, v. 65, no. 3, p. 227–248.

Hajian, H., 1977, Geological map of the Tafresh area: Tehran, Geological Survey of Iran, scale 1:100,000.

Hassanzadeh, J., 1993, Metallogenic and tectonomagmatic events in the SE sector of the Cenozoic active continental margin of central Iran (Shahr e Babak area, Keman Province): University of California, Los Angeles, unpublished Ph.D. dissertation, 204 p.

Huber, H., 1969a, Geological map of Iran, sheet no. 5, south-central Iran: National Iranian Oil Company, scale 1:1,000,000.

Huber, H., 1969b, Geological map of Iran, sheet no. 6 south-east Iran: National Iranian Oil Company, scale 1:1,000,000.

Huber, H., 1977, Geological map of Iran, sheet no. 2 south-east Iran: National Iranian Oil Company, scale 1:1,000,000.

Hunt, G.R., 1977, Spectral signatures of particulate minerals in the visible and near infrared: Geophysics, v. 42, no. 3, p. 501–513.

Hunt, G.R., and Ashley, R.P., 1979, Spectra of altered rocks in the visible and near infrared: Economic Geology , v. 74, no. 7, p. 1613–1629.

ImSpec LLC, 2004, ACORN 5.0 user's manual: ImSpec LLC, 122 p., accessed August 15, 2011, at http://www.imspec.com.

Iwasaki, A., and Tonooka, H., 2005, Validation of a crosstalk correction algorithm for ASTER/SWIR: Geoscience and Remote Sensing, IEEE Transactions, v. 43, no. 12, p. 2747−2751.

ITT, 2008, The Environment for Visualizing Images (ENVI) software: Boulder, Colorado, ITT Visual Information Solutions, accessed August 15, 2011, at http://www.ittvis.com/ProductServices/ENVI.aspx.

John, D.A., Ayuso, R.A., Barton, M.D., Blakely, R.J., Bodnar, R.J., Dilles, J.H., Gray, Floyd, Graybeal, F.T., Mars, J.C., McPhee, D.K., Seal, R.R., Taylor, R.D., and Vikre, P.G., 2010, Porphyry copper deposit model, chap. B *of* Mineral deposit models for resource assessment: U.S. Geological Survey Scientific Investigations Report 2010–5070–B, 169 p., accessed June 15, 2012, at http://pubs.usgs.gov/sir/2010/5070/b/.

Kruse, F.A., Boardman, J.W., and Huntington, J.F., 2003, Comparison of airborne hyperspectral data and EO-1 Hyperion for mineral mapping: Transactions on Geoscience and Remote Sensing, IEEE, v. 41, no. 6, p. 1388–1400.

Lowell, J.D., and Guilbert, J.M., 1970, Lateral and vertical alteration-mineralization zoning in porphyry ore deposits: Economic Geology, v. 65, no. 4, p. 373–408.

Mars, J.C., 2010, VINR-SWIR and TIR remote sensing of porphyry copper deposits, *in* John, D.A., Ayuso, R.A., Barton, M.D., Blakely, R.J., Bodnar, R.J., Dilles, J.H., Gray, Floyd, Graybeal, F.T., Mars, J.C., McPhee, D.K., Seal, R.R., Taylor, R.D., and Vikre, P.G., 2010, Porphyry copper deposit model, chap. B *of* Mineral deposit models for resource assessment: U.S. Geological Survey Scientific Investigations Report 2010–5070–B, p. 38–50, accessed June 15, 2012, at http://pubs.usgs.gov/sir/2010/5070/b/.

Mars, J.C., and Rowan, L.C., 2006, Regional mapping of phyllic- and argillic-altered rocks in the Zagros magmatic arc, Iran, using Advanced Spaceborne Thermal Emission and Reflection Radiometer (ASTER) data and logical operator algorithms: Geosphere, v. 2, p. 161–186, 2 plates.

Mars, J.C., and Rowan, L.C., 2007, Mapping phyllic and argillic-altered rocks in southeastern Afghanistan using Advanced Spaceborne Thermal Emission and Reflection Radiometer (ASTER) data: U.S. Geological Survey Open-File Report 2007–1006, 1 plate. (Also available at http://pdf.usaid.gov/pdf_docs/PNADI670.pdf.)

Mars, J.C., and Rowan, L.C., 2010, Spectral assessment of new ASTER SWIR surface reflectance data products for spectroscopic mapping of rocks and minerals: Remote Sensing of Environment, v. 114, p. 2011–2025.

National Aeronautics and Space Administration [NASA], 2003, Applied Sciences Directorate: National Aeronautics and Space Administration, accessed June 15, 2012, at https://zulu.ssc.nasa.gov/mrsid/.

Perelló, J., Razique, A., Schloderer, J., and Asad-Ur-Rehman, 2008, The Chagai porphyry copper belt, Baluchistan Province, Pakistan: Economic Geology, v. 103, p. 1583–1612.

Ranjbar, H., Shahriari, H., and Honarmand, M., 2004, Integration of ASTER and airborne geophysical data for exploration of copper mineralization—A case study of Sar Cheshmeh area: XXth International Society for Photogrammetry and Remote Sensing (ISPRS) Congress, 12–23 July 2004, Istanbul, Turkey, Commission 4, p. 701–706.

Regard, V., Bellier O., Thomas, J.-C., Abbassi M.R., Mercier, J., Shabanian, E., Feghhi, K., and Soleymani, S., 2004, Accommodation of Arabia-Eurasia convergence in the Zagros-Makran transfer zone, SE Iran—A transition between collision and subduction through a young deforming system: Tectonics, v. 23, no. 4, 24 p.

Rowan, L.C., and Mars, J.C., 2003, Lithologic mapping in the Mountain Pass, California area using Advanced Spaceborne Thermal Emission and Reflection Radiometer (ASTER) data: Remote Sensing of Environment, v. 84, no. 3, p. 350–366.

Rowan, L.C., Hook, S.J., Abrams, M.J., and Mars, J.C., 2003, Mapping hydrothermally altered rocks at cuprite, Nevada, using the advanced spaceborne thermal emission and reflection radiometer (ASTER), a new satellite-imaging system: Economic Geology, v. 98, no. 5 , p. 1019–1027.

Rowan, L.C., Schmidt, R.G., and Mars, J.C., 2006, Distribution of hydrothermally altered rocks in the Reko Diq, Pakistan mineralized area based on spectral analysis of ASTER data: Remote Sensing of the Environment, v. 104, p. 74–87.

Shamanian, G.H., Hedenquist, J.W., Hattori, K.H., and Hassanzadeh, J., 2004, The Gandy and Abolhassani epithermal prospects in the Alborz magmatic arc, Semnan Province, northern Iran: Economic Geology, v. 99, p. 691–712.

Singer, D.A., Berger, V.I., and Moring, B.C., 2008, Porphyry copper deposits of the World—Database and grade and tonnage models, 2008: U.S. Geological Survey Open-File Report 2008–1155, accessed June 1, 2011, at http://pubs.usgs.gov/of/2008/1155/.

Spatz, D.M., and Wilson, R.T., 1995, Remote sensing characteristics of porphyry copper systems, western America Cordillera, *in* Pierce, F.W., and Bolm, J.G., eds., Porphyry copper deposits of the American Cordillera: Arizona Geological Society Digest, v. 20, p. 94–108.

Stocklin, J., and Nabavi, M.H., 1973, Tectonic map of Iran: Tehran, Geological Survey of Iran, Offset Press Incorporated, scale 1:2,500,000.

Swayze, G.A., 1997, The hydrothermal and structural history of the Cuprite Mining District, southwestern Nevada—An integrated geological and geophysical approach: Boulder, Colorado, University of Colorado, unpublished Ph. D. dissertation, 399 p.

Taghizadeh, N. and Mallakpour, M.A., 1976, Mineral distribution map of Iran: Geological Survey of Iran, Tehran, Iran, scale 1:2,500,000.

Tangestani, M.H., and Moore, F., 2002, Porphyry copper alteration mapping at the Meiduk area, Iran: International Journal of Remote Sensing, v. 23, no. 22, p. 4815–4825.

Thome, K., Biggar, S., and Takashima, T., 1999, Algorithm Theoretical Basis Document For ASTER Level 2B1—Surface Radiance and ASTER Level 2B5—Surface Reflectance: The Earth Observing System, Goddard Space Flight Center, contract number: NAS5-31717, 45 p. (Also available online at http://eospso.gsfc.nasa.gov/eos_homepage/for_scientists/atbd/docs /ASTER/atbd-ast-07-09.pdf.)

Titley, S.R., 1972, Intrusion and wallrock porphyry copper deposits: Economic Geology, v. 67, p. 122.

Tucker, C.J., Grant, D.M., and Dykstra, J.D., 2004, NASA's global orthorectified Landsat dataset: Photogrammetric Engineering and Remote Sensing, v. 70, p. 313–322.

Valeh, N., 1972, Geological map of Iran, sheet 7647 Jebal Barez: Tehran, Geological Survey of Iran, Offset Press Incorporated, scale 1:100,000.

Waterman, G.C., and Hamilton, R.L., 1975, The Sar Cheshmeh porphyry copper deposit: Economic Geology, v. 70, p. 568–576.

Walker, R., and Jackson, J., 2001, Offset and evolution of the Gowk fault, S.E. Iran—A major intra-continental strike-slip system: Journal of Structural Geology, v. 24, p. 1677–1698.

Yamaguchi, Y., Fujisada, H., Kahle, A.B., Tsu, H., Kato, M., Watanabe, H., Sato, I., and Kudoh, M., 2001, ASTER instrument performance, operational status, and application to earth sciences: IEEE International, Geosciences and Remote Sensing Symposium, July 9–13, 2001, Sydney, Australia, doi: 10.1109/IGARSS.2001.976796.

Appendix A. ASTER Scene File Numbers

ASTER scene file numbers based on month, day, year, and time of acquisition, center of scene location in latitude and longitude, and calibration method used on the scene. ASTER scene file numbers correspond to index numbers for each ASTER scene in plate 1. (See Excel file available at http://pubs/usgs.gov/sir/2010/5090/o/.)

Appendix B. Potential Porphyry Copper Sites

Physical characteristics and location of potential porphyry copper sites. (See Excel file available at http://pubs/usgs.gov/sir/2010/5090/o/.)

Appendix C. Spatial Data Files

A file geodatabase (.gdb) and an ESRI map document (.mxd) are included with this report. The file geodatabase contains 5 feature classes. These may be downloaded from the U.S. Geological Survey website at http://pubs/usgs.gov/sir/2010/5090/o/ as zipped file **GIS_SIR2010-5090-O.zip**.

The file geodatabase is **Tethys_ASTER** and contains the following five feature classes:

SSIB_Tethys is a polygon feature class showing countries within and adjacent to the study area. The feature class is extracted from the country and shoreline boundaries maintained by the U.S. Department of State (2009).

Tethys_argillic is a polygon feature class that represents a hydrothermal mineral group consisting primarily of alunite and or kaolinite.

Tethys_ASTER_index is a polygon feature class that represents the ASTER scene outlines used to create argillic and phyllic feature classes.

Tethys_phyllic is a polygon feature class that represents a hydrothermal mineral consisting primarily of sericite.

Tethys_potential_deposits is a point feature class that represents sites that contain at least one or a combination of phyllic and argillic rocks that form surficial patterns and are associated with rock types typically found at porphyry copper deposits.

These feature classes are included in an ESRI map document (version 10, service pack 4) **Tethys_ASTER.mxd**.

Reference Cited

U.S. Department of State, 2009, Small-scale digital international land boundaries (SSIB)—Lines, edition 10, and polygons, beta edition 1, *in* Boundaries and sovereignty encyclopedia (B.A.S.E.): U.S. Department of State.

Menlo Park Publishing Service Center, California
Manuscript approved for publication November 1, 2013
Edited by Chet Zenone and James W. Hendley II and Jan Zigler and Sarah Nagorsen
Layout and design by James E. Banton

ISSN 2328-0328 (online)
http://dx.doi.org/10.3133/sir20105090O